Journal of
Materials Chemistry A

PAPER

View Article Online
View Journal | View Issue

Cite this: *J. Mater. Chem. A*, 2015, **3**, 19417

The accessibility of nitrogen sites makes a difference in selective CO_2 adsorption of a family of isostructural metal–organic frameworks†

Chengling Song,[a] Jiayi Hu,[a] Yajing Ling,[a] YunLong Feng,[a] Rajamani Krishna,*[b] De-li Chen*[c] and Yabing He*[a]

Received 18th July 2015
Accepted 10th August 2015

DOI: 10.1039/c5ta05481h

www.rsc.org/MaterialsA

By using three rigid diisophthalate organic linkers incorporating different numbers and orientations of Lewis basic nitrogen atoms into the spacers between two terminal isophthalate moieties, namely, 5,5′-(quinoline-5,8-diyl)-diisophthalate, 5,5′-(isoquinoline-5,8-diyl)-diisophthalate, and 5,5′-(quinoxaline-5,8-diyl)-diisophthalate, a family of isostructural copper-based metal–organic frameworks, **ZJNU-43**, **ZJNU-44** and **ZJNU-45**, were successfully solvothermally synthesized and structurally characterized by single-crystal X-ray diffraction. The three MOFs, after activation, exhibited almost the same porosities but distinctly different CO_2 adsorption properties. At room temperature and 1 atm, the adsorption capacities for CO_2 reached 103, 116 and 107 cm^3 (STP) g^{-1} for **ZJNU-43a**, **ZJNU-44a** and **ZJNU-45a**, respectively. Furthermore, Ideal Adsorbed Solution Theory (IAST) and simulated breakthrough analyses indicated that **ZJNU-44a** bearing much more easily accessible nitrogen sites is the best among the three MOFs for the separation of the following two binary gas mixtures at 296 K, *i.e.*, 50/50 CO_2/CH_4 and 15/85 CO_2/N_2 gas mixtures, indicating that the accessibility of nitrogen sites plays a much more crucial role, which is further confirmed by comprehensive quantum chemical calculations. The work demonstrates that the CO_2 adsorption properties of MOFs depend not only on the number of Lewis basic nitrogen sites but also more importantly on their accessibility.

Introduction

Carbon dioxide emitted through human activities is considered as the primary greenhouse gas causing global climate change. In addition, natural gas contains methane as its major component but also contains a certain amount of CO_2. The presence of CO_2 not only reduces the energy content of natural gas but also causes corrosion of pipelines and equipment during down and upstream natural gas processing. Therefore, effective capture and separation of CO_2 are thus becoming increasingly important for the reduction of CO_2 emission and upgradation of natural gas quality. The currently employed carbon capture method involves chemisorption by amine solution systems. However, amine regeneration requires cleavage of the N–C covalent bond formed between CO_2 and amine species by heating and thus has a high operational cost. In addition, volatile solvents might undergo degradation and loss during the operation, resulting in a negative environmental impact. In contrast, physisorption based separation is regarded as a very promising technology because of its low energy cost and high efficiency. However, the success of this approach is strongly dependent on the development of suitable porous adsorbents with very high adsorption selectivity and uptake capacity for CO_2. In this context, a new class of crystalline porous materials, metal–organic frameworks (MOFs),[1] also known as porous coordination polymers (PCPs),[2] assembled by bridging metal ions/clusters through organic linkers into extended networks, have shown promising potential because the pore sizes of MOFs can be tuned by the interplay of metal ions/metal containing clusters and organic linkers to enhance their size-selective separations, while the pore surfaces can be functionalized by the immobilization of specific sites to direct the recognition of CO_2 molecules. In fact, much research on MOFs has demonstrated their enormous potential for CO_2 storage and separation.[3]

---

[a] *College of Chemistry and Life Sciences, Zhejiang Normal University, Jinhua 321004, China. E-mail: heyabing@zjnu.cn*

[b] *Van't Hoff Institute for Molecular Sciences, University of Amsterdam, Science Park 904, 1098 XH Amsterdam, The Netherlands. E-mail: r.krishna@contact.uva.nl*

[c] *Key Laboratory of the Ministry of Education for Advanced Catalysis Materials, Institute of Physical Chemistry, Zhejiang Normal University, 321004 Jinhua, China. E-mail: chendl@zjnu.cn*

† Electronic supplementary information (ESI) available: PXRD patterns (Fig. S1–S3), TGA (Fig. S4), gas sorption isotherms (Fig. S5–S7), schematic of the breakthrough apparatus (Fig. S8), FTIR spectra (Fig. S9–S11), ^1H and ^{13}C NMR (Fig. S12), comparison of the textural properties of **ZJNU-43a**, **ZJNU-44a** and **ZJNU-45** (Table S1), single-site Langmuir fit parameters (Tables S3–S5), crystal data and structure refinement (Table S6). CCDC 1052691, 1052692, and 1055566. For ESI and crystallographic data in CIF or other electronic format see DOI: 10.1039/c5ta05481h

To improve the selective CO_2 adsorption, current efforts are largely devoted to enhancing the CO_2 binding affinity in MOFs. Reported strategies include creation of open metal sites, ligand functionalization, and construction of size/shape-specific pores. Among these methods, ligand functionalization, namely, adding specific functional groups into the organic linkers comprising MOFs by pre- or post-synthetic modification is widely performed, with its own advantages such as the chemical diversity of the available organic functional groups incorporated into MOFs. So far, various functional groups have been explored including OH, NH_2, NO_2, COOH, SO_3H, alkyl, alkoxy, halogen groups, amide, and heterocyclic moieties.[3g,3r,4] For example, Zhao *et al.* reported that hydroxyl and amino-functionalized MOFs exhibited enhanced CO_2 uptakes compared to the parent MOF.[4d] Also, Biswas demonstrated that the sulphonate-, carboxylate- and iodo-functionalized UiO-66 frameworks displayed higher adsorption selectivity for CO_2 over CH_4 compared to the unfunctionalized UiO-66 compound.[4b] Wang *et al.* synthesized a nitrogen-rich triazole functionalized MOF presenting exceptionally high uptake capacity for CO_2.[4c] The authors attributed the enhanced CO_2 adsorption capacity and selectivity to the favourable interactions between CO_2 molecules and the functional sites, namely, the electronic effect of functional groups. However, in design and development of MOF materials for CO_2 adsorption, one should not only consider the electronic effect of the functional groups, but more importantly the accessibility of functional groups should also be taken into account. It was envisaged that if these functional groups are blocked, they will have a limited effect on the improvement of CO_2 uptake capacities and adsorption selectivities. Although intuitive, the study in the aspect is less experimentally performed.

Based on the considerations and with the aim to understand how the accessibility of the Lewis basic nitrogen atoms may affect the adsorption properties of a given structure, in this study, we have targeted an isostructural family of MOFs bearing different numbers and orientations of nitrogen sites. The organic linkers outlined in Scheme 1, H_4L1–H_4L3, bearing different Lewis basic nitrogen numbers and orientations, were combined with paddlewheel dicopper $[Cu_2(COO)_4]$ secondary building units (SBUs) to construct three-dimensional (3D) NbO-type MOFs which we termed **ZJNU-43**, **ZJNU-44**, and **ZJNU-45**, respectively ("ZJNU" represents "Zhejiang Normal University"). The three MOFs are isostructural but differ only in the number and orientation of uncoordinated nitrogen atoms in the bridging ligands. Remarkably, systematic gas sorption studies on these materials show that the activated **ZJNU-44a** (hereafter, the letter "a" indicates activated MOF materials) bearing more exposed nitrogen atoms, albeit less nitrogen atoms than the one in **ZJNU-45a**, exhibits better CO_2 adsorption separation properties, indicating that the accessibility of nitrogen sites plays a more important role in CO_2 adsorption.

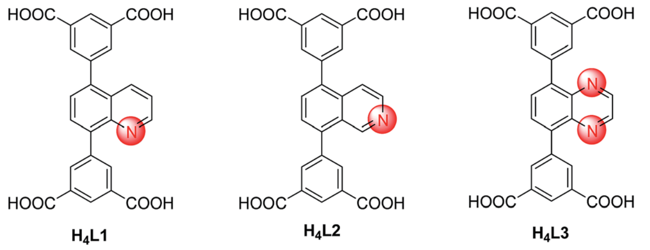

Scheme 1 The organic building blocks, H_4L1–H_4L3, used to construct MOFs ZJNU-43, ZJNU-44 and ZJNU-45.

Results and discussion

Synthesis and characterization

The organic ligands, H_4L1 to H_4L3, were synthesized by a cross-coupling reaction between dimethyl 5-(pinacolboryl)isophthalate and the corresponding dibromo derivatives followed by hydrolysis and acidification. The detailed synthetic procedures were provided in the Experimental section. The chemical structures of all the intermediates and ligands were characterized by NMR spectroscopy.

Solvothermal reactions of $Cu(NO_3)_2 \cdot 3H_2O$ with H_4L1 in a mixed solvent of *N*,*N*-dimethyl formamide (DMF)/EtOH/H_2O under acidic conditions at 353 K for 120 h afforded blue rhombic-shaped single crystals of **ZJNU-43** ($[Cu_2L1(H_2O)_2] \cdot 3DMF \cdot 2EtOH \cdot 4H_2O$). **ZJNU-44** ($[Cu_2L2(H_2O)_2] \cdot 3DMF \cdot 3CH_3CN \cdot 3H_2O$) was obtained by treating H_4L2 and $CuCl_2 \cdot 2H_2O$ in a mixed solvent of DMF/CH_3CN/H_2O under acidic conditions at 353 K for 72 h, while **ZJNU-45** ($[Cu_2L3(H_2O)_2] \cdot 3DMF \cdot 3MeOH \cdot 3H_2O$) was synthesized by a solvothermal reaction of H_4L3 and $Cu(NO_3)_2 \cdot 3H_2O$ in a mixed solvent of DMF/MeOH/H_2O under acidic conditions at 363 K for 48 h. Their structures were determined by single-crystal X-ray diffraction analyses, and the phase purity of the bulk crystalline materials was confirmed by a good match between the experimental and simulated powder X-ray diffraction patterns (Fig. S1–S3†). The formulae were established based on single-crystal X-ray structure determination, thermogravimetric analyses (TGA, Fig. S4†), and microanalysis.

Structural description

Single-crystal X-ray diffraction analyses showed that all the three compounds are isostructural, crystallizing in the trigonal space group $R\bar{3}m$. The crystal structure of **ZJNU-43** was representatively described. The two Cu centres are bridged by four carboxylate groups in a bis-monodentate fashion to form 4-connected square-planar $[Cu_2(COO)_4]$ SBUs, which link the 4-connected diisophthalate ligands to form a (4,4)-connected NbO-based 3D network. Alternatively, if the bridging organic linker is considered as having two 3-coordinated (3-c) branch points, then in combination with the 4-coordinated dicopper paddlewheels, the derived net is the one with the RCSR symbol fof.[5] The net topology is different with the one appearing in MOF NOTT-109 constructed from paddlewheel dicopper $[Cu_2(COO)_4]$ SBUs and 5,5-(naphthyl-1,4-diyl)-diisophthalate, although the used ligands are structurally similar,[6] indicating the tolerance of the NbO-net to the steric congestion imposed by ligand functionalization. In the framework, there exist two types of polyhedral nanocages which are stacked alternately through

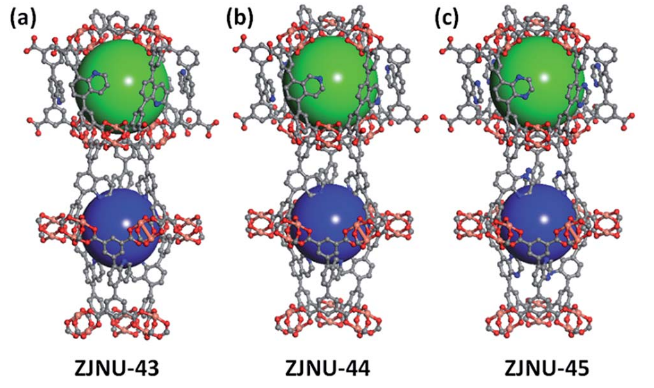

Fig. 1 Two different types of polyhedral nanocages in **ZJNU-43** (a), **ZJNU-44** (b) and **ZJNU-45** (c) decorated with different numbers and orientations of uncoordinated nitrogen atoms, which are shown in green and blue spheres, respectively. Hydrogen atoms and coordinated water molecules are omitted for clarity.

shared triangular windows along the crystallographic *c* axis. One cage shown in green sphere consists of 6 SBUs and 12 ligands, and the diameter is *ca.* 11.5 Å taking into account the van der Waals radius of the atoms, while the other one shown in blue sphere is constructed from 6 ligands and 12 SBUs with the dimensions of *ca.* 13 × 22 Å (Fig. 1a). The central quinolone ring is twisted from the plane defined by the two terminal isophthalates with a dihedral angle of 48.1°. The nitrogen atoms of the bridging ligands do not participate in the binding of Cu^{2+} ions, affording additional binding sites for the electron acceptor gases.

By comparison of the crystal structures of three MOFs (Fig. 1), it can be seen that the nitrogen atoms in **ZJNU-44** protrude into the pore which are much more easily accessible to the gas molecules, while the nitrogen atoms in **ZJNU-43** and **ZJNU-45** might be partially blocked by the neighbouring isophthalate moieties, which might lead to their different gas sorption properties.

Permanent porosities

The permanent porosities of the three compounds were established by nitrogen adsorption at 77 K. Prior to gas adsorption experiments, the samples were activated by solvent exchange with dry acetone followed by evacuation under dynamic vacuum at 373 K. The activated **ZJNU-43a**, **ZJNU-44a** and **ZJNU-45a** adsorbed a significant amount of N_2 gas at 77 K, showing typical type-I sorption isotherms, characteristics of microporous materials (Fig. 2a). Brunauer–Emmett–Teller (BET) surface areas were estimated by applying the BET equation, and pore volumes were calculated from the maximum amount of N_2 adsorbed. From the N_2 adsorption isotherms measured at 77 K, BET surface areas (pore volumes) were found to be 2243 m^2 g^{-1} (0.8943 cm^3 g^{-1}), 2314 m^2 g^{-1} (0.9158 cm^3 g^{-1}), and 2232 m^2 g^{-1} (0.8774 cm^3 g^{-1}) for **ZJNU-43a**, **ZJNU-44a** and **ZJNU-45a**, respectively (Table S1†). The results indicate that the three compounds have almost the same porosities even after the number of nitrogen atoms is increased or the orientation of nitrogen atoms is shifted.

Selective CO_2 adsorption

The successful incorporation of nitrogen heteroatom-containing building blocks into isostructural frameworks opens up a great opportunity toward delineating the relationships between the accessibility of nitrogen sites and gas adsorption performance. To investigate selective CO_2 adsorption properties of the three MOFs, single-component CO_2, CH_4 and N_2 gas sorption experiments were systematically carried out at 273 K and 296 K up to 1 atm, accordingly (Fig. S5–S7†). As shown in Fig. 2b, the CO_2 isotherms are completely reversible, indicating the fast adsorption and desorption kinetics. At 296 K, **ZJNU-43a** bearing the uncoordinated nitrogen atoms at the alpha (α) position in the spacer of the bridging ligands takes up CO_2 of 103 cm^3 (STP) g^{-1} under 1 atm. Interestingly, when the nitrogen atom is shifted from the α to beta (β) position, the resulting MOF **ZJNU-44a** shows a significant increase in CO_2 uptake capacity reaching 116 cm^3 (STP) g^{-1} under the same conditions. Furthermore, even though the number of the uncoordinated nitrogen atoms at the α position is increased from one to two, the resultant MOF **ZJNU-45a** adsorbs much lower amounts of CO_2 (107 cm^3 (STP) g^{-1}) than **ZJNU-44a**. Compared to **ZJNU-43a** and **ZJNU-**

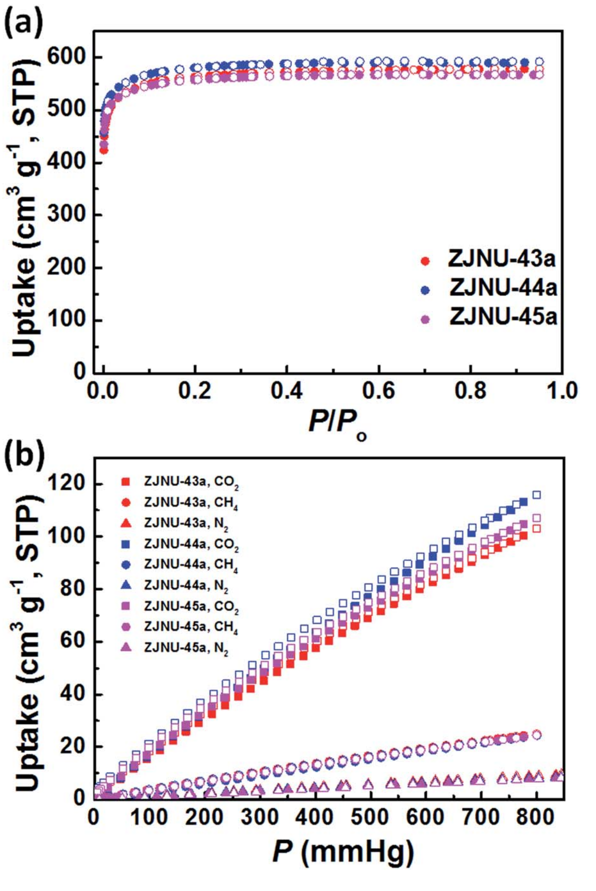

Fig. 2 (a) N_2 adsorption–desorption isotherms of **ZJNU-43a** (red), **ZJNU-44a** (blue) and **ZJNU-45a** (magenta) at 77 K. Solid and open symbols represent adsorption and desorption, respectively. (b) CO_2, CH_4, and N_2 sorption isotherms of **ZJNU-43a** (red), **ZJNU-44a** (blue) and **ZJNU-45a** (magenta) at 296 K. Solid and open symbols represent adsorption and desorption, respectively.

45a, the significant increase in CO_2 uptake capacity observed in **ZJNU-44a** is believed to stem from the uncoordinated nitrogen atoms pointing to the pore and thus being more easily accessible toward the incoming CO_2 gas molecules. These results indicate that the less blocked nitrogen site is beneficial for enhancing the CO_2 adsorption amount.

Most significantly, the three MOFs adsorbed much more CO_2 gas than CH_4, and N_2 (Fig. 2b), indicating the potential for selective CO_2 capture. Since the Ideal Adsorbed Solution Theory (IAST) method[7] has been shown to predict well mixed gas behaviour in MOFs from single-component isotherms,[8] we employed it to calculate the adsorption selectivities and CO_2 uptake capacities of the three MOFs for the separation of the following two binary gas mixtures: 50/50 CO_2/CH_4 and 15/85 CO_2/N_2. These mixtures mimic natural gas purification and post-combustion capture applications, respectively. Fig. 3a presents the values of adsorption selectivities as a function of the bulk pressure for 50/50 CO_2/CH_4 gas mixtures maintained under isothermal conditions at 296 K in the three MOFs. It can be seen that **ZJNU-44a** and **ZJNU-45a** have much higher selectivity towards CO_2 than **ZJNU-43a** in the entire pressure range measured. **ZJNU-44a** exhibits higher selectivity towards CO_2 than **ZJNU-45a** under pressure below 80 kPa. The CO_2/CH_4 adsorption selectivity of **ZJNU-44a** is *ca.* 5.5, which is similar to those observed in amine-substituted MOFs IRMOF-1$(NH_2)_4$ where the selectivity ranges from 5 to 6.[9] Fig. 3b presents the values of adsorption selectivities as a function of the bulk pressure for 15/85 CO_2/N_2 gas mixtures maintained under isothermal conditions at 296 K in the three MOFs. **ZJNU-45a** exhibits the highest selectivity towards CO_2 for adsorption from 15/85 CO_2/N_2 gas mixtures.

Besides adsorption selectivity, uptake capacity is equally important for a MOF applied as a gas separation material. Fig. 4a and b present IAST calculations for CO_2 uptakes from (a) 50/50 CO_2/CH_4 and (b) 15/85 CO_2/N_2 gas mixtures maintained under isothermal conditions at 296 K in **ZJNU-43a**, **ZJNU-44a**, and **ZJNU-45a**. For both mixtures, the lowest uptake of CO_2 is with **ZJNU-43a**.

The combination of higher adsorption selectivity and higher uptake capacity for CO_2 is most desirable and leads to enhanced separations in fixed beds. On the basis of the IAST calculations presented in Fig. 3 and 4, we should expect the separation performance of **ZJNU-43a** to be poorer than that of **ZJNU-44a** and **ZJNU-45a**. To confirm this expectation, we performed transient breakthrough simulations using the simulation methodology described in the literature.[8a,10] For the breakthrough simulations, the following parameter values were used: length of the packed bed, $L = 0.3$ m; voidage of the packed bed, $\varepsilon = 0.4$; superficial gas velocity at inlet, $u = 0.04$ m s^{-1}; see schematic in Fig. S8.† The transient breakthrough simulation results are presented in terms of a dimensionless time, τ, defined by dividing the actual time, t, by the characteristic time, $L\varepsilon/u$.

In natural gas purification processes, the primary objective is to produce CH_4 with a specified purity level, which is typically 500 ppm CO_2, *i.e.* 0.05 mol% CO_2. Let us compare the productivities of pure CH_4 that fulfils the specified impurity level for CO_2. Fig. 5a presents a comparison of the mol% CH_4 exiting the adsorber packed with **ZJNU-43a**, **ZJNU-44a**, and **ZJNU-45a** fed with 50/50 CO_2/CH_4 gas mixtures at 200 kPa total pressure and 296 K. During the time intervals, $\Delta\tau$, 99.95% + pure CH_4 can be produced. From the comparison presented in Fig. 5a, we conclude that the productivity of 99.95% + pure CH_4 is highest with **ZJNU-44a** and lowest with **ZJNU-43a**. This fulfils the expectations on the basis of the IAST calculations of adsorption selectivities and uptake capacities in the foregoing section.

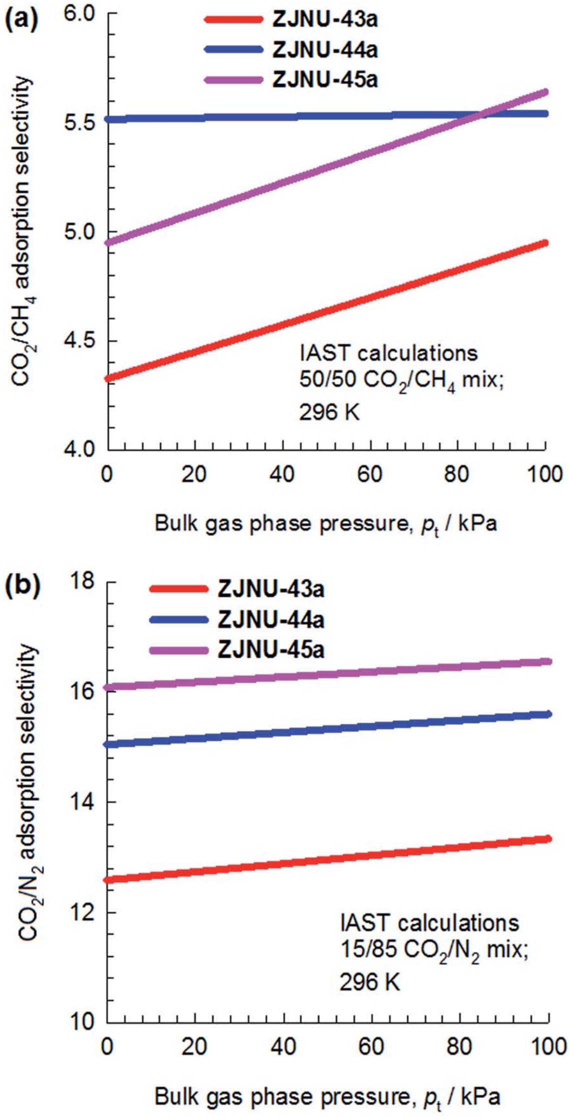

Fig. 3 Calculations using IAST of Myers and Prausnitz[7] for adsorption selectivities for (a) 50/50 CO_2/CH_4, and (b) 15/85 CO_2/N_2 gas mixtures maintained under isothermal conditions at 296 K in **ZJNU-43a** (red), **ZJNU-44a** (blue) and **ZJNU-45a** (magenta).

Next, we compare the separation of 15/85 CO_2/N_2 gas mixtures, which is relevant for CO_2 capture from flue gases. Fig. 5b presents a comparison of the mol% N_2 exiting the adsorber packed with **ZJNU-43a**, **ZJNU-44a**, and **ZJNU-45a** fed with 15/85 CO_2/N_2 gas mixtures at 100 kPa total pressure and 296 K. N_2 with a purity of 99.95% can be produced during the time intervals, $\Delta\tau$, as indicated in Fig. 5b. On the basis of the

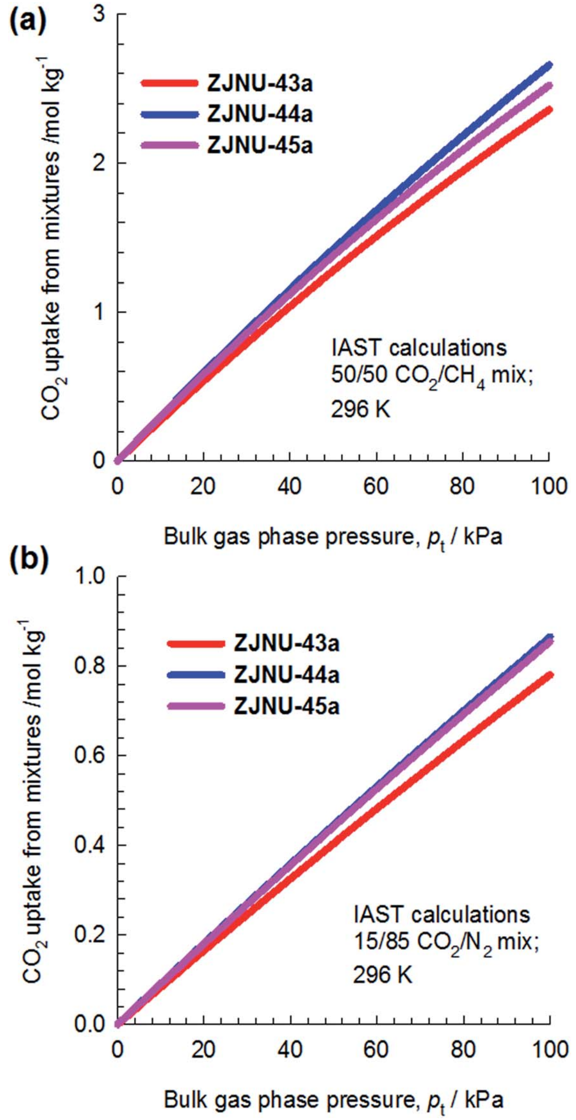

Fig. 4 Calculations using IAST of Myers and Prausnitz[7] for the uptake of CO_2 from (a) 50/50 CO_2/CH_4, and (b) 15/85 CO_2/N_2 gas mixtures maintained under isothermal conditions at 296 K in **ZJNU-43a** (red), **ZJNU-44a** (blue), and **ZJNU-45a** (magenta).

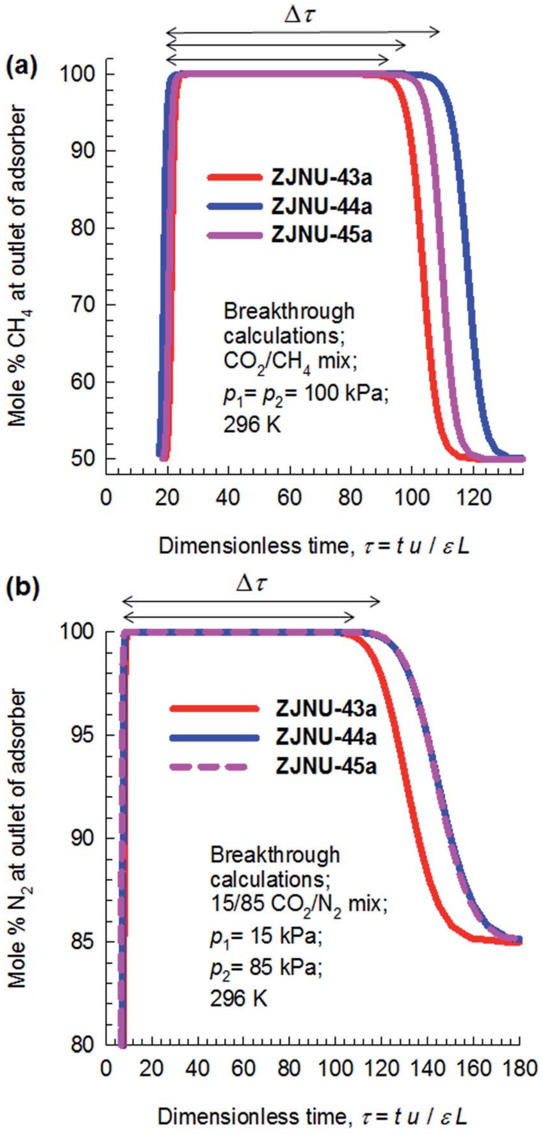

Fig. 5 (a) Comparison of the % CH_4 exiting the adsorber packed with **ZJNU-43a**, **ZJNU-44a**, and **ZJNU-45a** fed with 50/50 CO_2/CH_4 gas mixtures at 200 kPa total pressure and 296 K. (b) Comparison of the % N_2 exiting the adsorber packed with **ZJNU-43a**, **ZJNU-44a**, and **ZJNU-45a** fed with 15/85 CO_2/N_2 gas mixtures at 100 kPa total pressure and 296 K.

results, we conclude that the productivities of pure N_2 with a purity of 99.95% with **ZJNU-44a**, and **ZJNU-45a** are comparable, and higher than that with **ZJNU-43a**.

Taken together, IAST and simulated breakthrough analyses indicated that **ZJNU-44a** bearing much more easily accessible nitrogen sites outperform the other two MOFs for the separation of 50/50 CO_2/CH_4 and 15/85 CO_2/N_2 gas mixtures, indicating that the accessibility of nitrogen sites plays a much more crucial role.

Quantum chemical calculations

As discussed above, experimental data indicate that the MOF material **ZJNU-44a** has higher adsorption loading for CO_2 than **ZJNU-43a** and **ZJNU-45a**. However, the adsorption mechanism still remains unclear. The vdW corrected DFT-D2 method has been proved to be an effective tool to probe the occupation sites and orientations of the CO_2 molecule at various sites inside the framework, allowing us to better understand the adsorption mechanism. Therefore, we performed calculations to obtain binding energies of CO_2 starting from various configurations, and several typical occupation sites are obtained and listed in Fig. 6. The binding energy is calculated as:

$$E_{\mathrm{b}} = E_{\mathrm{gas/MOF}} - E_{\mathrm{gas}} - E_{\mathrm{MOF}}$$

where $E_{\mathrm{gas/MOF}}$, E_{gas}, and E_{MOF} represent the energies for CO_2 adsorbed **ZJNU-43** (**44**, **45**), isolated CO_2 molecule, and pure **ZJNU-43** (**44**, **45**) material, respectively. Three typical adsorption sites (triangular window site A, open metal site B, and N adsorption site C) are shown in Fig. 6, as well as their binding energies. Not surprisingly, the triangular window site (site A) for each material has a very strong adsorption affinity for the CO_2 molecule. The calculated E_b values for **ZJNU-43**, **44**, and **45** are almost the same, *i.e.*, −25.1, −26.1, and −26.1 kJ mol^{-1}, respectively, which is due to their very similar chemical environments at the triangular window sites. The distances between CO_2 and the atoms on the framework (*e.g.*, O and H atoms, see Fig. 6) surrounding the window are listed in Fig. 6, and we conclude that the CO_2 orientations at site A in the three MOF materials are almost the same. For each material, the open metal site (site B) has a much lower binding energy compared to the site A. For example, the E_b of CO_2 at site B in **ZJNU-43** (structure **B-ZJNU-43** in Fig. 6) is −11.8 kJ mol^{-1}, much smaller than the value of −25.1 kJ mol^{-1} for the structure **A-ZJNU-43**. Our calculations show that the binding energies of CO_2 at the same open metal site in **ZJNU-44** and **ZJNU-45** are −12.8 and −12.2 kJ mol^{-1}, respectively, very close to −11.8 kJ mol^{-1} in **ZJNU-43.** It is reasonable that three MOF materials have almost the same binding energies for CO_2 adsorption at the sites A and B, since the environment of the adsorption sites are the same. Therefore, we speculate that the CO_2 binding energies at the open N sites are different.

The open N sites in the three MOF materials have different environments, especially for **ZJNU-44**, where the open N is more accessible for gas molecule occupation, while the other two materials, **ZJNU-43** and **ZJNU-45**, have the same N orientations. As shown in Fig. 6, the CO_2 molecule is trapped in a very narrow window in structures **C-ZJNU-43** and **C-ZJNU-45**, forming many hydrogen bonds between CO_2 and the open N, H and O atoms on the framework. In the structure **C-ZJNU-43**, there are several weak bonds such as N⋯C (CO_2) with a distance of 2.87 Å and C (CO_2)–O with a distance of 2.80 Å, and several hydrogen bonds such as O (CO_2)⋯H with distances of 2.77 and 2.89 Å. The calculated binding energy at this site is about −18.2 kJ mol^{-1}, much stronger than that at the open metal site, suggesting that this is also an important adsorption site for the CO_2 molecule. In contrast, in the **ZJNU-44a** framework, the N site points to the pore and thus is completely available for occupation. The optimized structure **C-ZJNU-44** shows that the CO_2 molecule parallelly bridges to the organic ligand, forming three weak bonds, C (CO_2)–N, O (CO_2)–H, and O (CO_2)–H with distances of 2.85, 3.09 and 3.17 Å, respectively. Also, the O (CO_2) atom forms a hydrogen bond with the H atom surrounding the pore with a distance of 2.91 Å. Surprisingly, the calculated E_b is −27.6 kJ mol^{-1}, even larger than the E_b value of −26.1 kJ mol^{-1} at the triangular window site, and also much larger than those of −18.1 and −18.7 kJ mol^{-1} in **C-ZJNU-43** and **C-ZJNU-45**, respectively. Compared to the N at the α site, the N at the more open β site prevails on CO_2 adsorption, and thus well explains the larger adsorption loading in **ZJNU-44.** Furthermore, the double N sites in **ZJNU-45** lead to more available sites for CO_2 adsorption compared to **ZJNU-43**, which is in accordance with the larger CO_2 loading for **ZJNU-45.** Our calculations confirm that rational design of the open N sites in the framework could effectively enhance CO_2 adsorption.

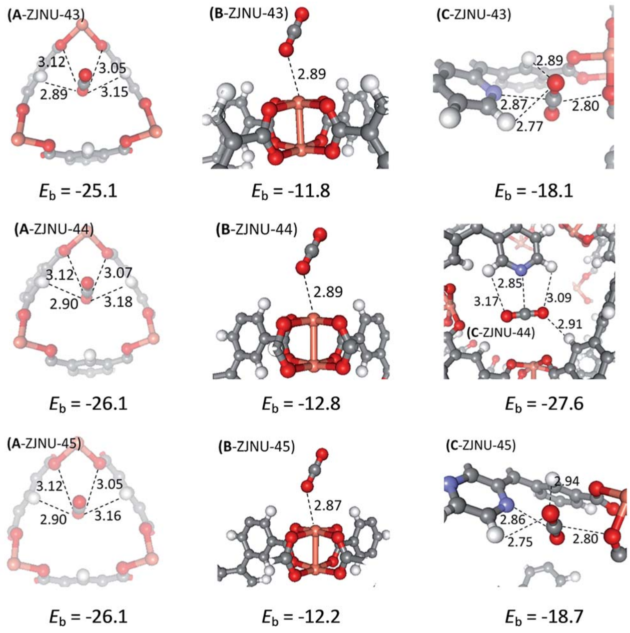

Fig. 6 Three optimized structures representing the typical adsorption sites for CO_2 in ZJNU-43, ZJNU-44, and ZJNU-45 are shown, as well as several hydrogen bond lengths and the DFT-D2 computed binding energy for each configuration. The units for bond distance and binding energy are Å and kJ mol^{-1}, respectively. A, B, and C represent the window site, open metal site, and N adsorption site, respectively. The O, H, C, Cu, and N atoms are represented with red, white, grey, brown, and blue balls, respectively.

Conclusions

In summary, we have designed and developed three nitrogen-containing diisophthalate organic ligands, and used them to construct three isostructural MOFs featuring different numbers and orientations of nitrogen sites. Gas adsorption studies showed that **ZJNU-44a** exhibited higher CO_2 adsorption capacities than **ZJNU-43a** and **ZJNU-45a** despite their similar porosities. Furthermore, IAST and simulated breakthrough calculations showed that **ZJNU-44a** performed better than the other two MOF materials for selective CO_2/CH_4 and CO_2/N_2 separations. Comprehensive DFT calculations indicated that the higher CO_2 adsorption capacities and better separation performance of **ZJNU-44a** is attributed to much more easily accessible nitrogen atoms in **ZJNU-44a,** indicating that the accessibility of nitrogen atoms plays a much more crucial role. This work demonstrates that rational design of open nitrogen sites will effectively enhance CO_2 adsorption, and thus provides useful information toward future design and synthesis of new MOF materials with improving CO_2 gas adsorption and separation capacity.

Experimental section

Materials and methods

All chemicals were purchased from commercial sources and used as received unless otherwise noted. MeOH (purity ≥ 99.5%), EtOH (purity ≥ 99.7%), CH_3CN (purity ≥ 99.0%), toluene (purity ≥ 99.5%), dioxane (purity ≥ 99.5%) and DMF (purity ≥ 98%) were obtained from Chinasun Specialty Products Co., Ltd. $Pd(PPh_3)_4$ (Pd, 9.2%) and DEF (purity ≥ 99%) were obtained from Beijing HWRK Chem Co.,Ltd. Cs_2CO_3 (purity ≥ 99%) was obtained from Shanghai Shaoyuan Co. Ltd. $Cu(NO_3)_2\cdot 3H_2O$ (99.0–102.0%) and $CuCl_2\cdot 2H_2O$ (≥99.0%) were obtained from Sinopharm Chemical Reagent Co., Ltd. 5,8-Dibromoquinoline,[11] 5,8-dibromoisoquinoline,[12] 5,8-dibromoquinoxaline[13] and dimethyl 5-(pinacolboryl)isophthalate[14] were synthesized according to the reported methods. Column chromatography was carried out on silica gel (100–200 mesh, Qingdao Haiyang Chemical Co., Ltd). Thin-Layer Chromatography (TLC) analyses were carried out using aluminium sheets pre-coated with silica gel 60 F254 purchased from Merck. The elemental analysis of C, H and N was performed on a Vario EL III CHNOS elemental analyser. Fourier transform infrared spectroscopy (FTIR) spectra were recorded on a Nicolet 5DX FT-IR spectrometer with samples in KBr pellets. Thermogravimetric analysis (TGA) was performed on a Netzsch STA 449C thermal analyzer with a heating rate of 5 °C min^{-1} in a flowing nitrogen atmosphere (10 mL min^{-1}). ^{1}H NMR and ^{13}C NMR spectra of the compounds were measured using a Bruke AVANCE 400 or 600 NMR spectrometer by dissolving the samples in DMSO-d_6 or $CDCl_3$. The chemical shifts were reported as parts per million (ppm) with use of residual solvent as an internal standard for ^{1}H (δ $CDCl_3$ = 7.26 ppm, δ DMSO-d_6 = 2.50 ppm) and ^{13}C spectra (δ $CDCl_3$ = 77.16 ppm, δ DMSO-d_6 = 39.52 ppm). Coupling constants are reported in Hz. Resonance patterns were reported with the notations of s (singlet), d (doublet), t (triplet) and m (multiplet). Powder X-ray diffraction (PXRD) patterns were recorded on a Philips PW3040/60 automated powder diffractometer, using Cu-K$_\alpha$ radiation (λ = 1.542 Å) in a 2θ range of 5–40°. An ASAP 2020 surface area analyser was used to measure the adsorption behaviours of N_2, CH_4, and CO_2. Before gas adsorption measurements, the sample was activated by solvent exchange with dry acetone, followed by evacuation at 373 K until the degas rate reached 5 μm Hg min^{-1}.

Single-crystal X-ray crystallography

The X-ray diffraction data were collected on a Agilent supernova dual diffractometer with Cu-K$_\alpha$ radiation (λ = 1.54178 Å). Absorption corrections were performed using a multi-scan method. The structure was solved by direct methods with SHELXS-97 (ref. 15) and refined with a full-matrix least-squares technique within the SHELXL program package. The unit cell includes a large region of disordered solvent molecules, which could not be modelled as discrete atomic sites. We employed PLATON/SQUEEZE[16] to calculate the diffraction contribution of the solvent molecules and, thereby, to produce a set of solvent-free diffraction intensities; structures were then refined again using the data generated. Hydrogen atoms of the ligand were calculated in ideal positions with isotropic displacement parameters, while H atoms of water molecules were not included in the final refinement. The crystal data and structure refinement results are listed in Table S6 in the ESI.†

Synthesis and characterization of the organic linkers

5,5′-(Quinolone-5,8-diyl)-diisophthalate (H_4L1). To a mixture of 5,8-dibromoquinoline (1.00 g, 3.48 mmol), dimethyl 5-(pinacolboryl)isophthalate (2.45 g, 7.67 mmol), Cs_2CO_3 (3.41 g, 10.45 mmol) and $Pd(PPh_3)_4$ (0.20 g, 0.18 mmol) was added dry dioxane (80 mL). The resulting mixture was stirred under reflux under a nitrogen atmosphere for 72 h. After the removal of the solvents, CH_2Cl_2 (100 mL) and H_2O (100 mL) were added. The mixture was filtered. The organic phase was separated and the aqueous phase was extracted with CH_2Cl_2. The combined organic phase was washed with brine, dried over anhydrous $MgSO_4$ and filtered. Volatiles were removed by roto-evaporation under reduced pressure and the residue was recrystallized with toluene to afford the tetramethyl intermediate. Yield: 1.44 g, 2.80 mmol, 81%. ^{1}H NMR ($CDCl_3$, 400.1 MHz) δ (ppm): 9.002 (dd, J = 1.6 Hz, 4.0 Hz, 1H), 8.831 (t, J = 1.6 Hz, 1H), 8.787 (t, J = 1.6 Hz, 1H), 8.639 (d, J = 1.6 Hz, 2H), 8.408 (d, J = 1.6 Hz, 2H), 8.193 (dd, J = 1.6, 8.8 Hz, 1H), 7.873 (d, J = 7.6 Hz, 1H), 7.646 (d, J = 7.2 Hz, 1H), 7.464 (dd, J = 4.0 Hz, 8.8 Hz, 1H), 4.016 (s, 6H), 4.003 (s, 6H).

To a suspension of the tetramethyl intermediate (1.44 g, 2.80 mmol) in THF (20 mL) and MeOH (20 mL) was added 6 M NaOH (20 mL, 120 mM). The resulting mixture was refluxed overnight. After the removal of the solvents, the residue was dissolved in water, and acidified with conc. HCl under an ice-water bath. The resulting precipitate was collected by filtration, and dried in a vacuum at 70 °C, affording the target compound in a quantitative yield. ^{1}H NMR (DMSO-d_6, 600.1 MHz) δ (ppm): 8.989 (dd, J = 4.2, 1.2 Hz, 1H), 8.596 (t, J = 1.8 Hz, 1H), 8.548 (t, J = 1.8 Hz, 1H), 8.486 (d, J = 1.2 Hz, 2H), 8.273 (d, J = 1.8 Hz, 2H), 8.252 (dd, J = 1.2 Hz, 8.4 Hz, 1H), 7.970 (d, J = 7.8 Hz, 1H), 7.755 (d, J = 7.2 Hz, 1H), 7.619 (dd, J = 4.2 Hz, 8.4 Hz, 1H); ^{13}C NMR (DMSO-d_6, 150.9 MHz) δ (ppm): 167.154, 166.854, 151.098, 145.580, 140.253, 139.763, 138.849, 138.531, 135.866, 134.859, 134.220, 132.346, 131.405, 130.401, 129.827, 129.285, 128.019, 126.564, 122.699.

5,5′-(Isoquinoline-5,8-diyl)-diisophthalate (H_4L2). To a mixture of 5,8-dibromoisoquinoline (0.50 g, 1.74 mmol), dimethyl 5-(pinacolboryl)isophthalate (1.23 g, 3.83 mmol), Cs_2CO_3 (1.70 g, 5.23 mmol) and $Pd(PPh_3)_4$ (0.10 g, 0.09 mmol) was added dry dioxane (60 mL). The resulting mixture was stirred under reflux under a nitrogen atmosphere for 72 h. After the removal of the solvents, CH_2Cl_2 (100 mL) and H_2O (100 mL) were added. The mixture was filtered. The organic phase was separated and the aqueous phase was extracted with CH_2Cl_2. The combined organic phase was washed with brine, dried over anhydrous $MgSO_4$ and filtered. Volatiles were removed by roto-evaporation under reduced pressure and the residue was purified using silica gel column chromatography with petroleum ether/CH_2Cl_2/ethyl acetate (2/2/1, v/v/v) as eluent, affording the tetramethyl intermediate. Yield: 0.67 g, 1.30 mmol, 75.0%; ^{1}H NMR ($CDCl_3$, 400.1 MHz) δ (ppm): 9.279 (s, 1H), 8.858 (t, J = 1.6 Hz, 1H), 8.839 (t, J = 1.6 Hz, 1H), 8.598 (t, J = 6.0 Hz, 1H), 8.454 (d, J = 1.6 Hz, 2H), 8.419 (d, J = 1.6 Hz, 2H), 7.773 (d, J = 7.2 Hz, 1H), 7.663 (t, J = 7.2 Hz, 2H), 4.020 (s, 6H), 4.016 (s, 6H).

To a suspension of the tetramethyl intermediate (0.67 g, 1.30 mmol) in THF (20 mL) and MeOH (20 mL) was added 6 M NaOH

(20 mL, 120 mM). The resulting mixture was refluxed overnight. After the removal of the solvents, the residue was dissolved in water, and acidified with conc. HCl under an ice-water bath. The precipitation was collected by filtration, and dried in a vacuum at 70 °C to afford the target compound in a quantitative yield. ^{1}H NMR (DMSO-d_6, 600.1 MHz) δ (ppm): 9.195 (s, 1H), 8.603 (t, J = 1.8 Hz, 1H), 8.589 (t, J = 1.8 Hz, 1H), 8.577 (d, J = 6.0 Hz, 1H), 8.327 (d, J = 1.8 Hz, 2H), 8.280 (d, J = 1.2 Hz, 2H), 7.907 (d, J = 7.2 Hz, 1H), 7.777 (d, J = 7.2 Hz, 1H), 7.716 (d, J = 6.0 Hz, 1H); ^{13}C NMR (DMSO-d_6, 150.1 MHz) δ (ppm): 166.815, 150.529, 144.112, 139.416, 139.111, 138.842, 137.187, 134.934, 134.788, 134.063, 132.398, 132.350, 131.705, 130.043, 129.906, 129.019, 126.360, 118.320.

5,5′-(Quinoxaline-5,8-diyl)-diisophthalate (H_4L3). To a mixture of 5,8-dibromoquinoxaline (0.29 g, 0.99 mmol), dimethyl 5-(pinacolboryl)isophthalate (0.70 g, 2.18 mmol), Cs_2CO_3 (0.97 g, 2.98 mmol) and $Pd(PPh_3)_4$ (0.06 g, 0.05 mmol) was added dry dioxane (40 mL). The resulting mixture was stirred under reflux under a nitrogen atmosphere for 72 h. After the removal of the solvents, CH_2Cl_2 (40 mL) and H_2O (40 mL) were added. The mixture was filtered. The organic phase was separated and the aqueous phase was extracted with CH_2Cl_2. The combined organic phase was washed with brine, dried over anhydrous $MgSO_4$ and filtered. Volatiles were removed by evaporation under reduced pressure and the residue was recrystallized with toluene to afford the tetramethyl intermediate. Yield: 0.39 g, 0.076 mmol, 77%. ^{1}H NMR ($CDCl_3$, 600.1 MHz) δ (ppm): 8.957 (s, 2H), 8.817 (t, J = 1.8 Hz, 2H), 8.620 (d, J = 1.8 Hz, 4H), 7.992 (s, 2H), 4.019 (s, 12H).

To a suspension of the tetramethyl intermediate (0.39 g, 0.076 mmol) in THF (20 mL) and MeOH (20 mL) was added 6 M NaOH (20 mL, 120 mM). The resulting mixture was refluxed overnight. After the removal of the solvents, the residue was dissolved in water, and acidified with conc. HCl under an ice-water bath. The precipitation was collected by filtration, and dried in a vacuum at 70 °C to afford the target compound in a quantitative yield. ^{1}H NMR (DMSO-d_6, 400.1 MHz) δ (ppm): 9.035 (s, 2H), 8.555 (t, J = 1.6 Hz, 2H), 8.479 (d, J = 1.6 Hz, 4H), 8.088 (s, 2H); ^{13}C NMR (DMSO-d_6, 100.6 MHz) δ (ppm): 167.034, 145.967, 140.408, 138.960, 138.853, 135.809, 131.614, 130.941, 129.596.

Synthesis and characterization of the MOFs

ZJNU-43. A mixture of the organic linker H_4L1 (5.0 mg, 10.93 μmol) and $Cu(NO_3)_2 \cdot 3H_2O$ (15.0 mg, 62.10 μmol) was dissolved in a mixed solvent of DMF, ethanol and H_2O (1.5 mL/0.5 mL/0.08 mL) in a screw-capped vial (20 mL). After 80 μL of 6 M HCl were added, the vial was capped and heated at 353 K for 120 h. Blue rhombic crystals were obtained in 63% yield. **ZJNU-43** can be best formulated as $[Cu_2L1(H_2O)_2] \cdot 3DMF \cdot 2C_2H_5OH \cdot 4H_2O$ on the basis of single-crystal X-ray diffraction structure determination, TGA and microanalysis. Selected FTIR (KBr, cm^{-1}): 1655, 1637, 1630, 1502, 1439, 1387, 1369, 1302, 1254, 1097, 1049, 918, 862, 777, 756, 731, 661, 494; anal. for $C_{38}H_{56}Cu_2N_4O_{19}$, calcd: C 45.64%, H 5.64%, N 5.60%; found: C 45.59%, H 5.57%, N 5.55%.

ZJNU-44. A mixture of the organic linker H_4L2 (5.0 mg, 10.93 μmol) and $CuCl_2 \cdot 2H_2O$ (10.0 mg, 58.66 μmol) was dissolved in a mixed solvent of DMF, acetonitrile and H_2O (1.5 mL/0.5 mL/0.08 mL) in a screw-capped vial (20 mL). After 50 μL of 6 M HCl were added, the vial was capped and heated at 353 K for 72 h. Blue rhombic crystals were obtained in 53% yield. **ZJNU-44** can be best formulated as $[Cu_2L2(H_2O)_2] \cdot 3DMF \cdot 3CH_3CN \cdot 3H_2O$ on the basis of single-crystal X-ray diffraction structure determination, TGA and microanalysis. Selected FTIR (KBr, cm^{-1}): 1655, 1570, 1439, 1413, 1373, 1306, 1254, 1099, 1053, 777, 756, 731, 694, 661, 492; anal. for $C_{40}H_{51}Cu_2N_7O_{16}$, calcd: C 47.43%, H 5.07%, N 9.68%; found: C 47.39%, H 5.15%, N 9.54%.

ZJNU-45. A mixture of the organic linker H_4L3 (5.0 mg, 10.91 μmol) and $Cu(NO_3)_2 \cdot 3H_2O$ (15.0 mg, 62.10 μmol) was dissolved in a mixed solvent of DMF, methanol and H_2O (1.5 mL/0.5 mL/0.08 mL) in a screw-capped vial (20 mL). 50 μL of 6 M HCl were then added. The vial was capped and heated at 363 K for 48 h. Blue rhombic crystals were obtained in 60% yield. **ZJNU-45** can be best formulated as $[Cu_2L3(H_2O)_2] \cdot 3DMF \cdot 3MeOH \cdot 3H_2O$ on the basis of single-crystal X-ray diffraction structure determination, TGA and microanalysis. Selected FTIR (KBr, cm^{-1}): 1655, 1578, 1439, 1419, 1383, 1362, 1298, 1254, 1101, 1049, 777, 756, 729, 488; anal. for $C_{36}H_{53}Cu_2N_5O_{19}$, calcd: C 43.81%, H 5.41%, N 7.10%; found: C 43.79%, H 5.49%, N 6.91%.

Fitting of pure component isotherms

The measured experimental data on excess loadings, q_{excess}, of the pure components CO_2, CH_4, and N_2 in **ZJNU-43a**, **ZJNU-44a**, and **ZJNU-45a** were first converted to absolute loadings, q, using

$$q = q^{\text{excess}} + \frac{pV_{\text{pore}}}{ZRT} \tag{1}$$

where Z is the compressibility factor. The Peng–Robinson equation of state was used to estimate Z. The accessible pore volumes are provided in Table S1.†

The absolute component loadings were fitted with the Langmuir model

$$q = q_{\text{sat}} \frac{bp}{1+bp} \tag{2}$$

with T-dependent parameter b

$$b = b_0 \exp\left(\frac{E}{RT}\right) \tag{3}$$

where q (mol kg^{-1}) is the adsorbed amount, p (Pa) is the equilibrium pressure, q_{sat} (mol kg^{-1}) is the monolayer adsorption capacity, and b (Pa^{-1}) is the Langmuir adsorption equilibrium constant. The Langmuir parameters for the adsorption of CO_2 are provided in Tables S2–S4† for **ZJNU-43a**, **ZJNU-44a** and **ZJNU-45a**, respectively.

Isosteric heat of adsorption

The isosteric heat of adsorption, Q_{st}, was determined using the pure-component isotherm fits using the Clausius–Clapeyron equation, defined as

$$Q_{\mathrm{st}} = RT^2 \left(\frac{\partial \ln p}{\partial T} \right)_q \tag{4}$$

where p (Pa) is the pressure, T (K) is the temperature, R is the gas constant, and q (mol kg^{-1}) is the adsorption amount.

IAST calculations of adsorption selectivities and uptake capacities

The selectivity of preferential adsorption of component 1 over component 2 in a mixture containing 1 and 2, perhaps in the presence of other components too, can be formally defined as

$$S_{\mathrm{ads}} = \frac{q_1/q_2}{p_1/p_2} \tag{5}$$

In eqn (5), q_1 and q_2 are the absolute component loadings of the adsorbed phase in the mixture. These component loadings are also termed the uptake capacities. We calculate the values of q_1 and q_2 using the IAST of Myers and Prausnitz.[7]

Quantum chemical calculations

All of the periodic density functional theory (DFT) calculations were performed using the Vienna *ab initio* simulation package with a version of vasp.5.3.3.[17] The van der Waals (vdW) corrected DFT method, DFT-D2,[18] was employed to capture the weak vdW forces between CO_2 and the three materials. The Brillouin zone was sampled with gamma point only, which is sufficient for the calculations of CO_2 binding energies since the values are almost unchanged by increasing Monkhorst-Pack grids[19] in our test calculations. In all of our calculations a planewave energy cutoff of 500 eV was employed. The experimental unit cells of **ZJNU-43**, **ZJNU-44**, and **ZJNU-45** are reduced to primitive cells (**ZJNU-43**: $a = b = c = 16.79$ Å, $\alpha = \beta = \gamma = 67.27°$; **ZJNU-44**: $a = b = c = 16.77$ Å, $\alpha = \beta = \gamma = 67.57°$; **ZJNU-45**: $a = b = c = 16.75$ Å, $\alpha = \beta = \gamma = 67.28°$) for the sake of computational efficiency. The lattice constants are fixed while all of the atoms are allowed to relax using the DFT-D2 method. Note that it is reasonable to fix the lattice constants in our calculations since the relaxation of the lattice constants only slightly changes the values, which should have a negligible effect on the CO_2 binding energies. For the optimizations of adsorbates/**ZJNU-43** (**44**, **45**), all of the atoms were relaxed until the force on each ion was less than 0.01 eV Å^{-1}.

Acknowledgements

Y. He acknowledges financial support from the National Natural Science Foundation of China (No. 21301156), and Open Research Fund of Top Key Discipline of Chemistry in Zhejiang Provincial Colleges and Key Laboratory of the Ministry of Education for Advanced Catalysis Materials (ZJHX201313). D.-L. Chen thanks financial support from the National Natural Science foundation of China (NSFC grant No. 21303165).

References

1 O. M. Yaghi, G. Li and H. Li, *Nature*, 1995, **378**, 703–706.

2 S. Kitagawa, R. Kitaura and S.-i. Noro, *Angew. Chem., Int. Ed.*, 2004, **43**, 2334–2375.

3 (*a*) Z. Hu, Y. Peng, Z. Kang, Y. Qian and D. Zhao, *Inorg. Chem.*, 2015, **54**, 4862–4868; (*b*) S.-J. Bao, R. Krishna, Y.-B. He, J.-S. Qin, Z.-M. Su, S.-L. Li, W. Xie, D.-Y. Du, W.-W. He, S.-R. Zhang and Y.-Q. Lan, *J. Mater. Chem. A*, 2015, **3**, 7361–7367; (*c*) Z. Zhang, Z.-Z. Yao, S. Xiang and B. Chen, *Energy Environ. Sci.*, 2014, **7**, 2868–2899; (*d*) R.-J. Li, M. Li, X.-P. Zhou, D. Li and M. O'Keeffe, *Chem. Commun.*, 2014, **50**, 4047–4049; (*e*) B. Wang, H. Huang, X.-L. Lv, Y. Xie, M. Li and J.-R. Li, *Inorg. Chem.*, 2014, **53**, 9254–9259; (*f*) P.-Q. Liao, H. Chen, D.-D. Zhou, S.-Y. Liu, C.-T. He, Z. Rui, H. Ji, J.-P. Zhang and X.-M. Chen, *Energy Environ. Sci.*, 2015, **8**, 1011–1016; (*g*) N. H. Alsmail, M. Suyetin, Y. Yan, R. Cabot, C. P. Krap, J. Lü, T. L. Easun, E. Bichoutskaia, W. Lewis, A. J. Blake and M. Schröder, *Chem.–Eur. J.*, 2014, **20**, 7317–7324; (*h*) Y. Xie, H. Yang, Z. U. Wang, Y. Liu, H.-C. Zhou and J.-R. Li, *Chem. Commun.*, 2014, **50**, 563–565; (*i*) Y. Li, Z. Ju, B. Wu and D. Yuan, *Cryst. Growth Des.*, 2013, **13**, 4125–4130; (*j*) E. Yang, H.-Y. Li, F. Wang, H. Yang and J. Zhang, *CrystEngComm*, 2013, **15**, 658–661; (*k*) C. Hou, Q. Liu, P. Wang and W.-Y. Sun, *Microporous Mesoporous Mater.*, 2013, **172**, 61–66; (*l*) P. Nugent, Y. Belmabkhout, S. D. Burd, A. J. Cairns, R. Luebke, K. Forrest, T. Pham, S. Ma, B. Space, L. Wojtas, M. Eddaoudi and M. J. Zaworotko, *Nature*, 2013, **495**, 80–84; (*m*) Z. Zhang, Y. Zhao, Q. Gong, Z. Li and J. Li, *Chem. Commun.*, 2013, **49**, 653–661; (*n*) Q. Yang, V. Guillerm, F. Ragon, A. D. Wiersum, P. L. Llewellyn, C. Zhong, T. Devi, C. Serre and G. Maurin, *Chem. Commun.*, 2012, **48**, 9831–9833; (*o*) J. Park, Z. U. Wang, L.-B. Sun, Y.-P. Chen and H.-C. Zhou, *J. Am. Chem. Soc.*, 2012, **134**, 20110–20116; (*p*) J.-R. Li, J. Sculley and H.-C. Zhou, *Chem. Rev.*, 2012, **112**, 869–932; (*q*) K. Sumida, D. L. Rogow, J. A. Mason, T. M. McDonald, E. D. Bloch, Z. R. Herm, T.-H. Bae and J. R. Long, *Chem. Rev.*, 2012, **112**, 724–781; (*r*) B. Li, Z. Zhang, Y. Li, K. Yao, Y. Zhu, Z. Deng, F. Yang, X. Zhou, G. Li, H. Wu, N. Nijem, Y. J. Chabal, Z. Lai, Y. Han, Z. Shi, S. Feng and J. Li, *Angew. Chem., Int. Ed.*, 2012, **51**, 1412–1415; (*s*) R. Vaidhyanathan, S. S. Iremonger, G. K. H. Shimizu, P. G. Boyd, S. Alavi and T. K. Woo, *Science*, 2010, **330**, 650–653; (*t*) S. R. Caskey, A. G. Wong-Foy and A. J. Matzger, *J. Am. Chem. Soc.*, 2008, **130**, 10870–10871; (*u*) R. Banerjee, A. Phan, B. Wang, C. Knobler, H. Furukawa, M. O'Keeffe and O. M. Yaghi, *Science*, 2008, **319**, 939–943; (*v*) Y.-S. Bae, O. K. Farha, A. M. Spokoyny, C. A. Mirkin, J. T. Hupp and R. Q. Snurr, *Chem. Commun.*, 2008, 4135–4137.

4 (*a*) M. Zhang, Q. Wang, Z. Lu, H. Liu, W. Liu and J. Bai, *CrystEngComm*, 2014, **16**, 6287–6290; (*b*) S. Biswas, J. Zhang, Z. Li, Y.-Y. Liu, M. Grzywa, L. Sun, D. Volkmer and P. Van Der Voort, *Dalton Trans.*, 2013, **42**, 4730–4737; (*c*) X.-J. Wang, P.-Z. Li, Y. Chen, Q. Zhang, H. Zhang, X. X. Chan, R. Ganguly, Y. Li, J. Jiang and Y. Zhao, *Sci.*

Rep., 2013, **3**, 1149; (*d*) Y. Zhao, H. Wu, T. J. Emge, Q. Gong, N. Nijem, Y. J. Chabal, L. Kong, D. C. Langreth, H. Liu, H. Zeng and J. Li, *Chem.–Eur. J.*, 2011, **17**, 5101–5109.

5 (*a*) Y. He, B. Li, M. O'Keeffe and B. Chen, *Chem. Soc. Rev.*, 2014, **43**, 5618–5656; (*b*) M. Li, D. Li, M. O'Keeffe and O. M. Yaghi, *Chem. Rev.*, 2014, **114**, 1343–1370; (*c*) V. Guillerm, D. Kim, J. F. Eubank, R. Luebke, X. Liu, K. Adil, M. S. Lah and M. Eddaoudi, *Chem. Soc. Rev.*, 2014, **43**, 6141–6172.

6 X. Lin, I. Telepeni, A. J. Blake, A. Dailly, C. M. Brown, J. M. Simmons, M. Zoppi, G. S. Walker, K. M. Thomas, T. J. Mays, P. Hubberstey, N. R. Champness and M. Schröder, *J. Am. Chem. Soc.*, 2009, **131**, 2159–2171.

7 A. L. Myers and J. M. Prausnitz, *AIChE J.*, 1965, **11**, 121–127.

8 (*a*) E. D. Bloch, W. L. Queen, R. Krishna, J. M. Zadrozny, C. M. Brown and J. R. Long, *Science*, 2012, **335**, 1606–1610; (*b*) Z. R. Herm, J. A. Swisher, B. Smit, R. Krishna and J. R. Long, *J. Am. Chem. Soc.*, 2011, **133**, 5664–5667; (*c*) R. Krishna and J. M. v. Baten, *J. Membr. Sci.*, 2011, **377**, 249–260; (*d*) R. Krishna and J. M. v. Baten, *J. Membr. Sci.*, 2011, **383**, 289–300.

9 W. Mu, D. Liu, Q. Yang and C. Zhong, *Microporous Mesoporous Mater.*, 2010, **130**, 76–82.

10 (*a*) Y. He, R. Krishna and B. Chen, *Energy Environ. Sci.*, 2012, **5**, 9107–9120; (*b*) R. Krishna and J. R. Long, *J. Phys. Chem. C*, 2011, **115**, 12941–12950.

11 M. Tomar, N. T. Lucas, H. Kim, F. Laquai, K. Müllen and J. Jacob, *Polym. Int.*, 2012, **61**, 1318–1325.

12 W. D. Brown and A. H. Gouliaev, *Synthesis*, 2002, 83–86.

13 S. Jo, D. Kim, S.-H. Son, Y. Kim and T. S. Lee, *ACS Appl. Mater. Interfaces*, 2014, **6**, 1330–1336.

14 C. Song, Y. Ling, Y. Feng, W. Zhou, T. Yildirim and Y. He, *Chem. Commun.*, 2015, **51**, 8508–8511.

15 G. M. Sheldrick, *Acta Crystallogr., Sect. A: Cryst. Phys., Diffr., Theor. Gen. Crystallogr.*, 2008, **64**, 112–122.

16 A. L. Spek, *J. Appl. Crystallogr.*, 2003, **36**, 7–13.

17 (*a*) G. Kresse and J. Furthmüller, *Phys. Rev. B: Condens. Matter Mater. Phys.*, 1996, **54**, 11169–11186; (*b*) G. Kresse and J. Furthmüller, *Comput. Mater. Sci.*, 1996, **6**, 15–50; (*c*) G. Kresse, *J. Non-Cryst. Solids*, 1995, **193**, 222–229; (*d*) G. Kresse and J. Hafner, *Phys. Rev. B: Condens. Matter Mater. Phys.*, 1994, **49**, 14251–14264.

18 S. Grimme, *J. Comput. Chem.*, 2006, **27**, 1787–1799.

19 H. J. Monkhorst and J. D. Pack, *Phys. Rev. B: Condens. Matter Mater. Phys.*, 1976, **13**, 5188–5192.

Electronic Supplementary Material (ESI) for Journal of Materials Chemistry A.

The Accessibility of Nitrogen Sites Makes Difference to Selective CO_2 Adsorption in a Family of Isostructural Metal-Organic Frameworks

Chengling Song,[a] Jiayi Hu,[a] Yajing Ling,[a] Yunlong Feng,[a] Rajamani Krishna,[b*] De-li Chen[c*] and Yabing He[a*]

[a.] College of Chemistry and Life Sciences, Zhejiang Normal University, Jinhua 321004, China. E-mail: heyabing@zjnu.cn

[b.] Van't Hoff Institute for Molecular Sciences, University of Amsterdam Science Park 904, 1098 XH Amsterdam, The Netherlands. E-mail: r.krishna@uva.nl

[c.] Key Laboratory of the Ministry of Education for Advanced Catalysis Materials, Institute of Physical Chemistry, Zhejiang Normal University, 321004 Jinhua, China. E-mail: chendl@zjnu.cn

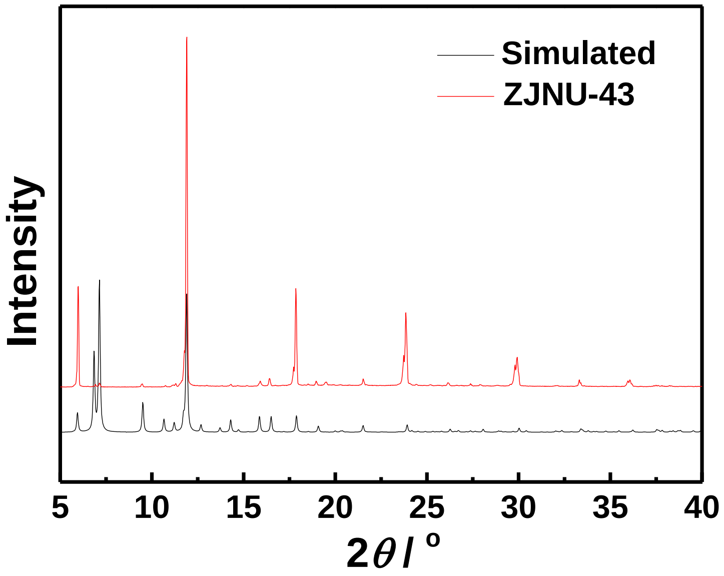

Figure S1. PXRD pattern of as-synthesized MOF **ZJNU-43** together with the one simulated from cif file. Calculated PXRD patterns were generated using Mercury 1.4.1.

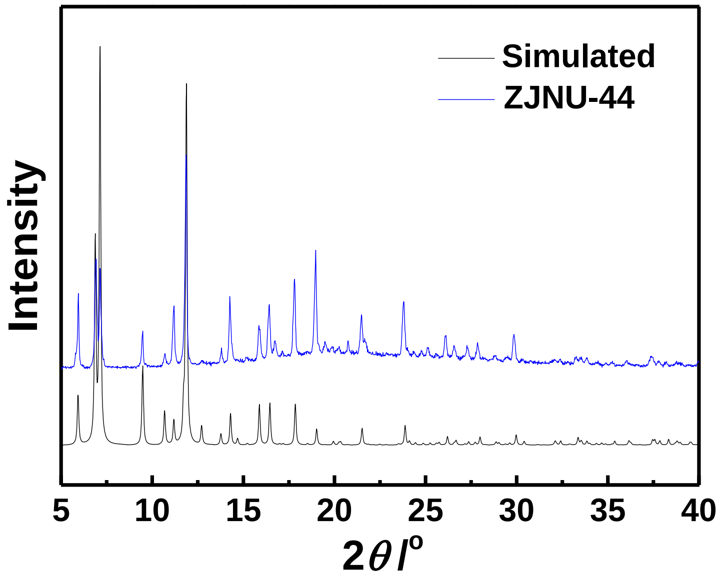

Figure S2. PXRD pattern of the as-synthesized MOF **ZJNU-44** together with the one simulated from its cif file. Calculated PXRD patterns were generated using Mercury 1.4.1.

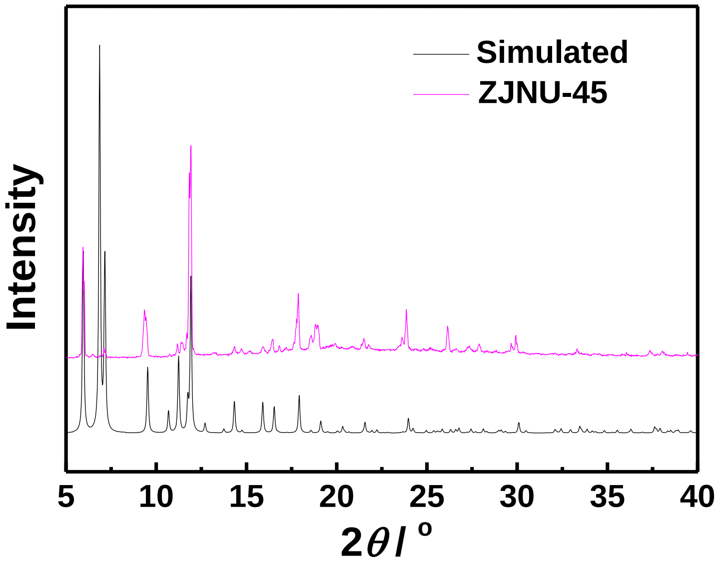

Figure S3. PXRD pattern of the as-synthesized MOF **ZJNU-45** together with the one simulated from its cif file. Calculated PXRD patterns were generated using Mercury 1.4.1.

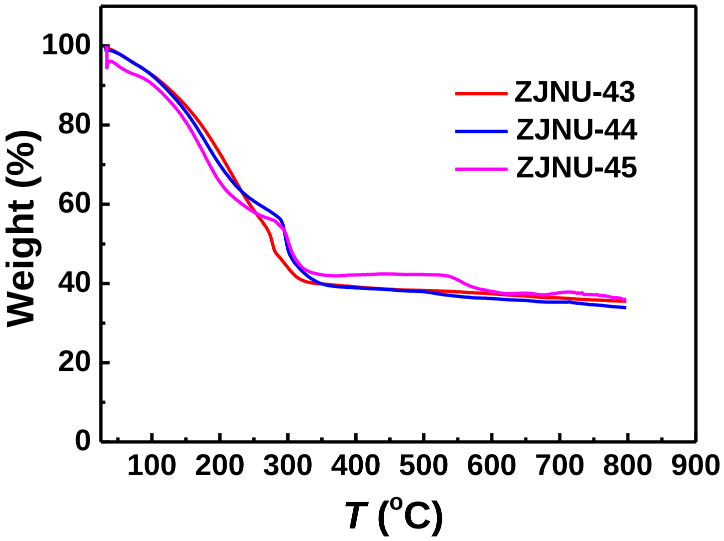

Figure S4. TGA curves of as-synthesized MOFs **ZJNU-43** (red)**, ZJNU-44** (blue) and **ZJNU-45** (magenta) under a nitrogen atmosphere with a heating rate of 5 ^{o}C min^{-1}.

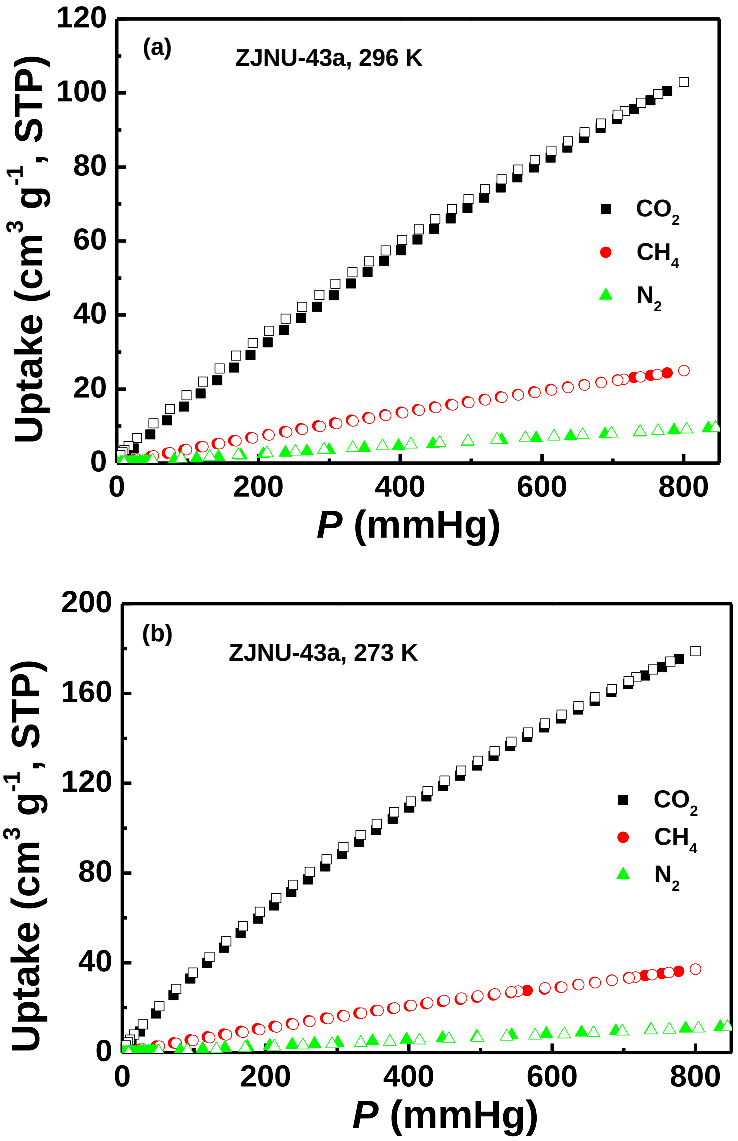

Figure S5. CO_2, CH_4 and N_2 sorption isotherms of **ZJNU-43a** at 296 K (a) and 273 K (b). Solid and open symbols represent adsorption and desorption, respectively.

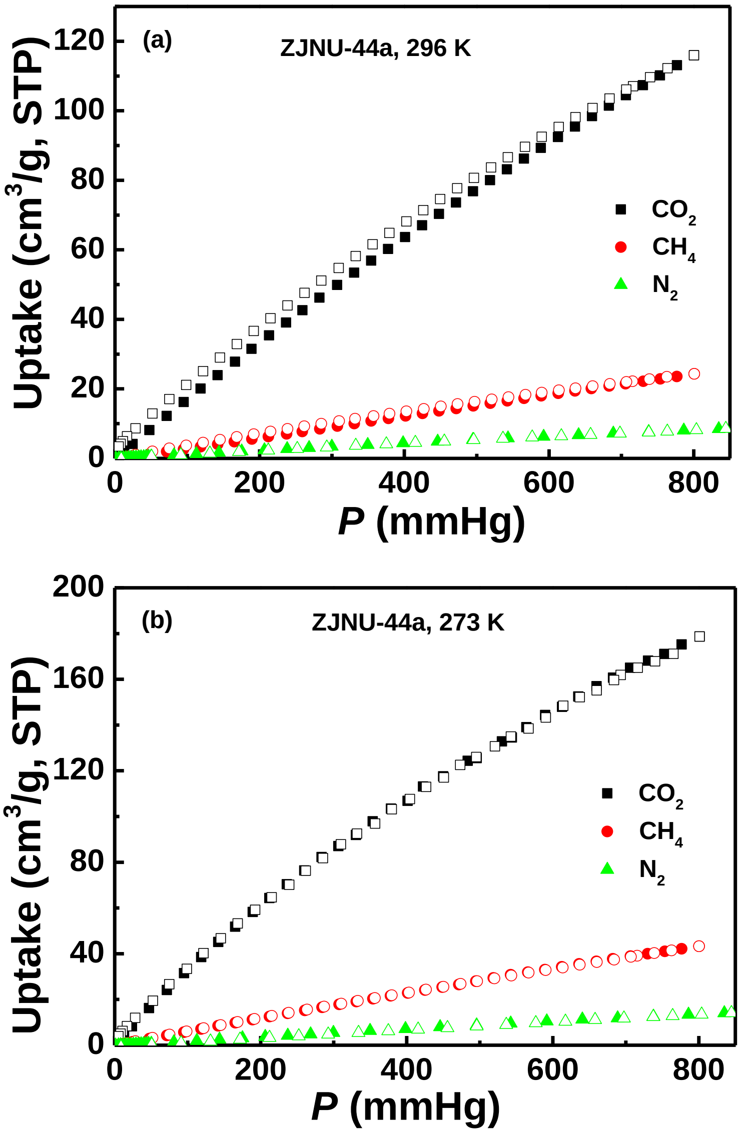

Figure S6. CO_2, CH_4 and N_2 sorption isotherms of **ZJNU-44a** at 296 K (a) and 273 K (b). solid and open symbols represent adsorption and desorption, respectively.

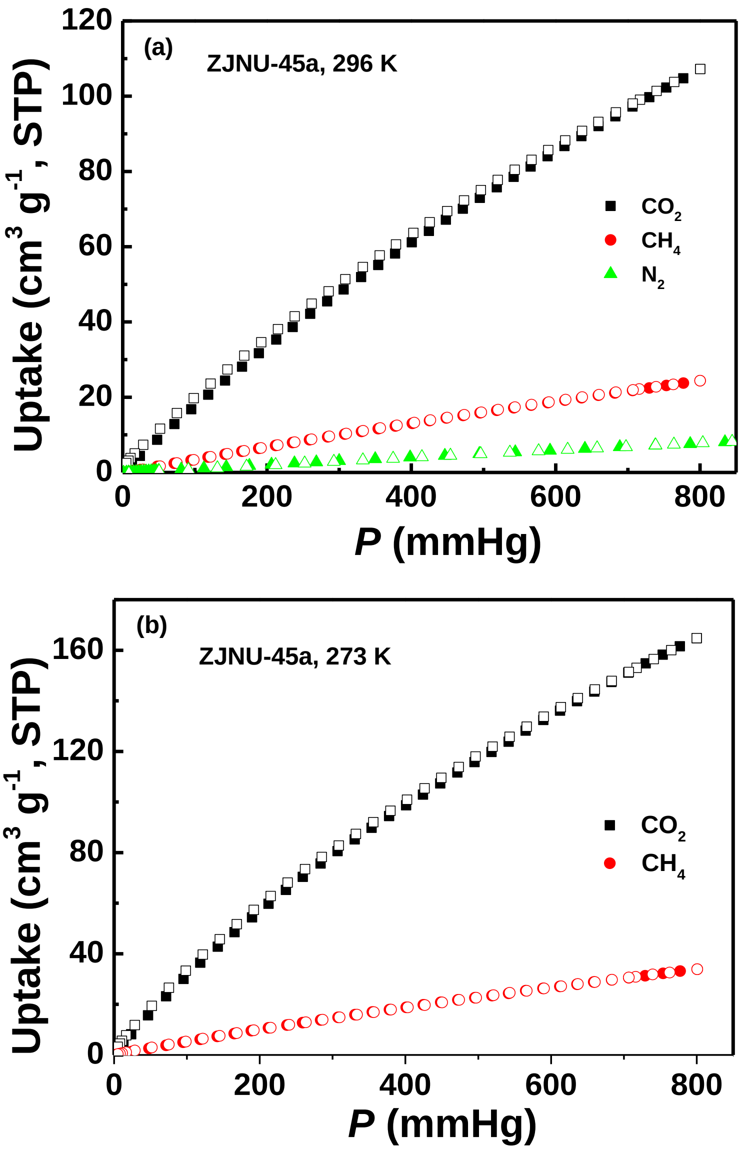

Figure S7. CO_2, CH_4 and N_2 sorption isotherms of **ZJNU-45a** at 296 K (a) and 273 K (b). Solid and open symbols represent adsorption and desorption, respectively.

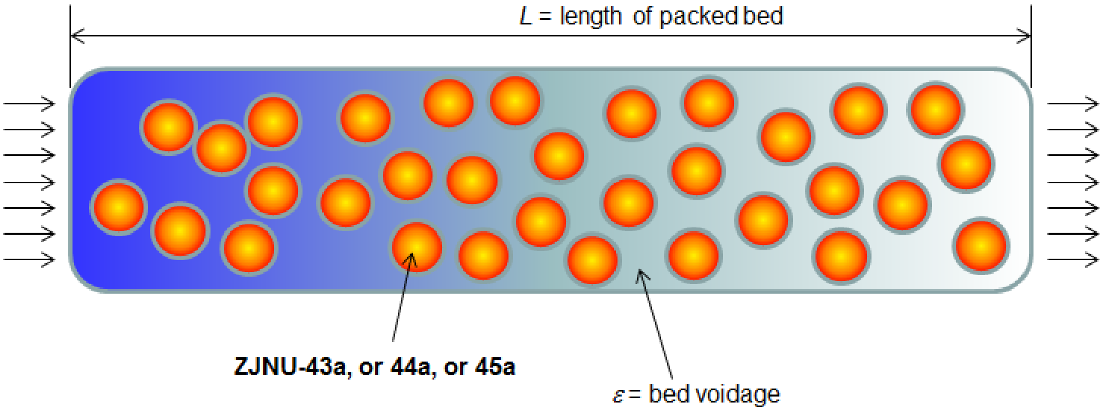

Figure S8. Schematic of the breakthrough apparatus. The length L = 0.3 m. The apparatus is operated at 296 K, and at a total gas pressure P = 200 kPa. The bed porosity, ε = 0.4. The interstitial gas velocity, u = 0.04 m s^{-1}.

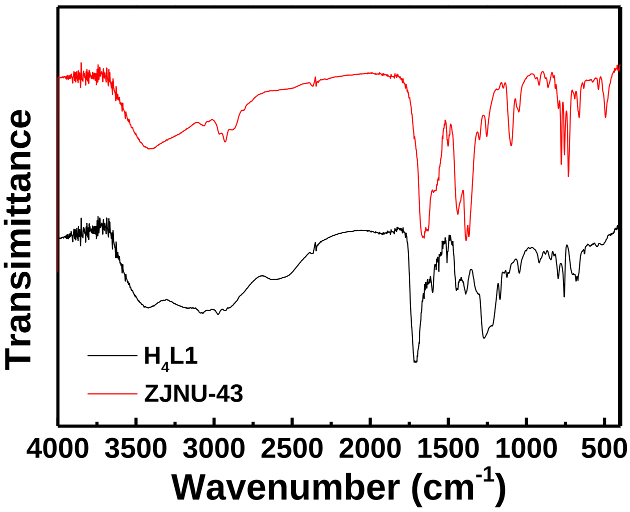

Figure S9. FTIR spectra of the organic linker H_4L1 and the as-synthesized MOF **ZJNU-43**.

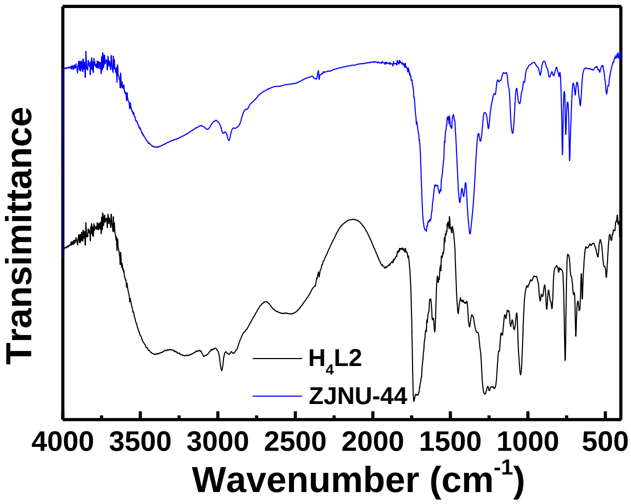

Figure S10. FTIR spectra of the organic linker H_4L2 and the as-synthesized MOF **ZJNU-44**.

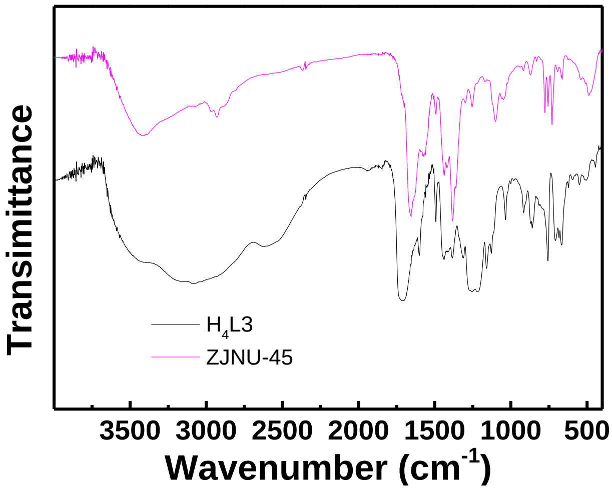

Figure S11. FTIR spectra of the organic linker H_4L3 and the as-synthesized MOF **ZJNU-45**.

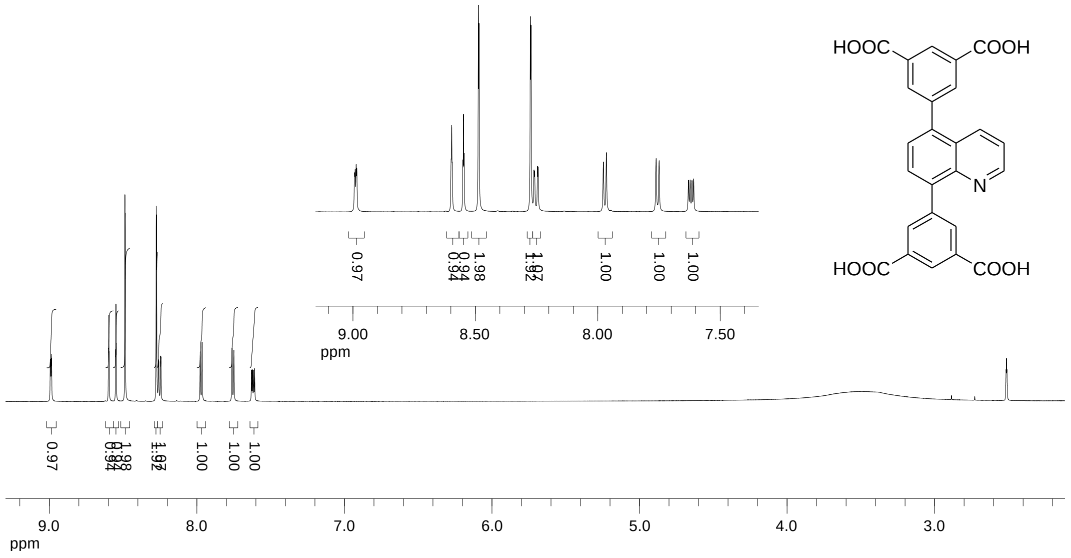
HOOC
COOH
N
HOOC
COOH
0.97
0.94
0.94
1.98
1.92
1.97
1.00
1.00
1.00
9.00
8.50
8.00
7.50
ppm
9.0
8.0
7.0
6.0
5.0
4.0
3.0
ppm

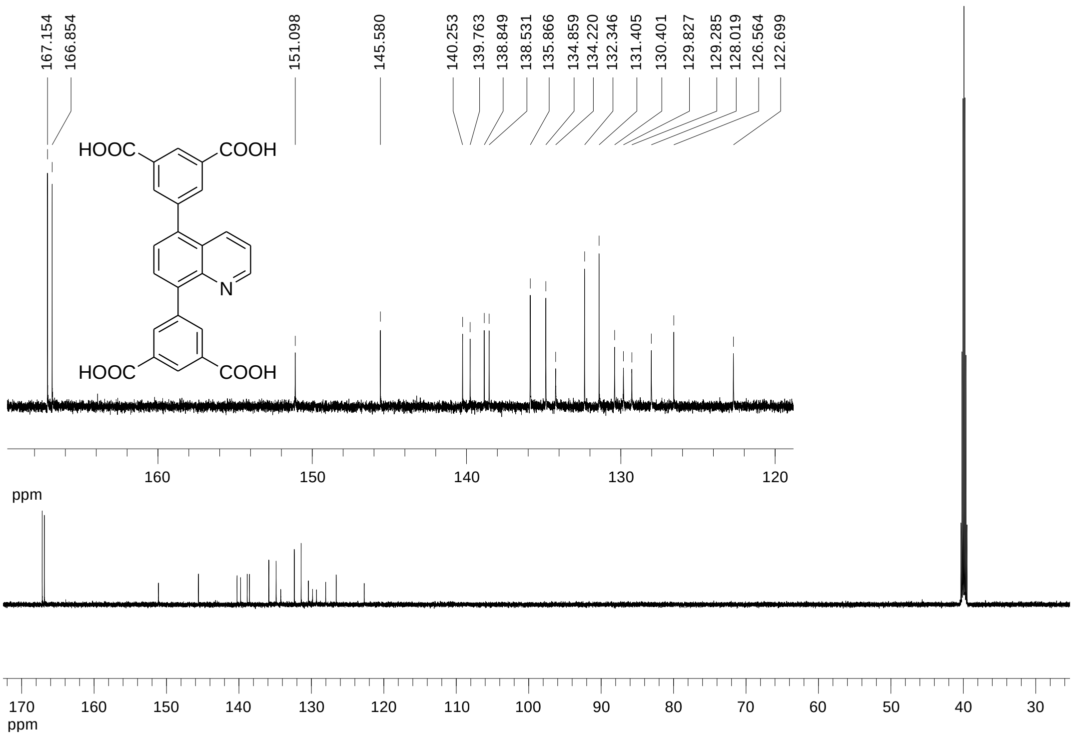
167.154
166.854
151.098
145.580
140.253
139.763
138.849
138.531
135.866
134.859
134.220
132.346
131.405
130.401
129.827
129.285
128.019
126.564
122.699
HOOC
COOH
N
HOOC
COOH
160
150
140
130
120
ppm
170
160
150
140
130
120
110
100
90
80
70
60
50
40
30
ppm

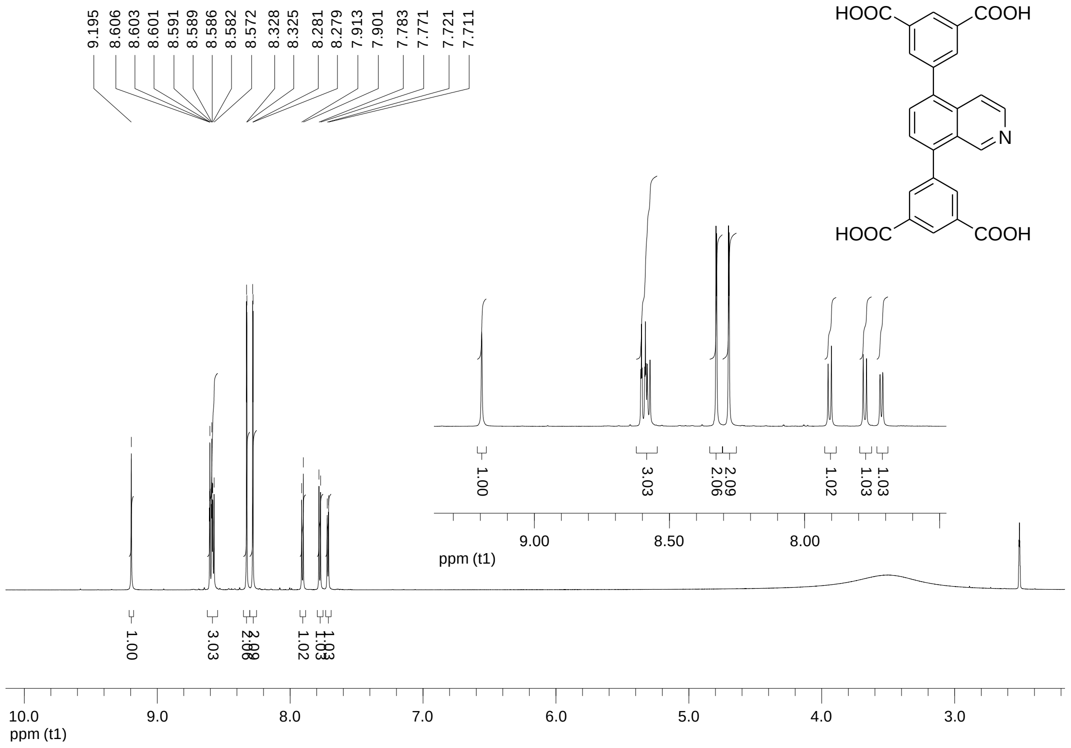
9.195
8.606
8.603
8.601
8.591
8.589
8.586
8.582
8.572
8.328
8.325
8.281
8.279
7.913
7.901
7.783
7.771
7.721
7.711
HOOC
COOH
N
HOOC
COOH
1.00
3.03
2.06
2.09
1.02
1.03
1.03
9.00
8.50
8.00
ppm (t1)
10.0
9.0
8.0
7.0
6.0
5.0
4.0
3.0
ppm (t1)

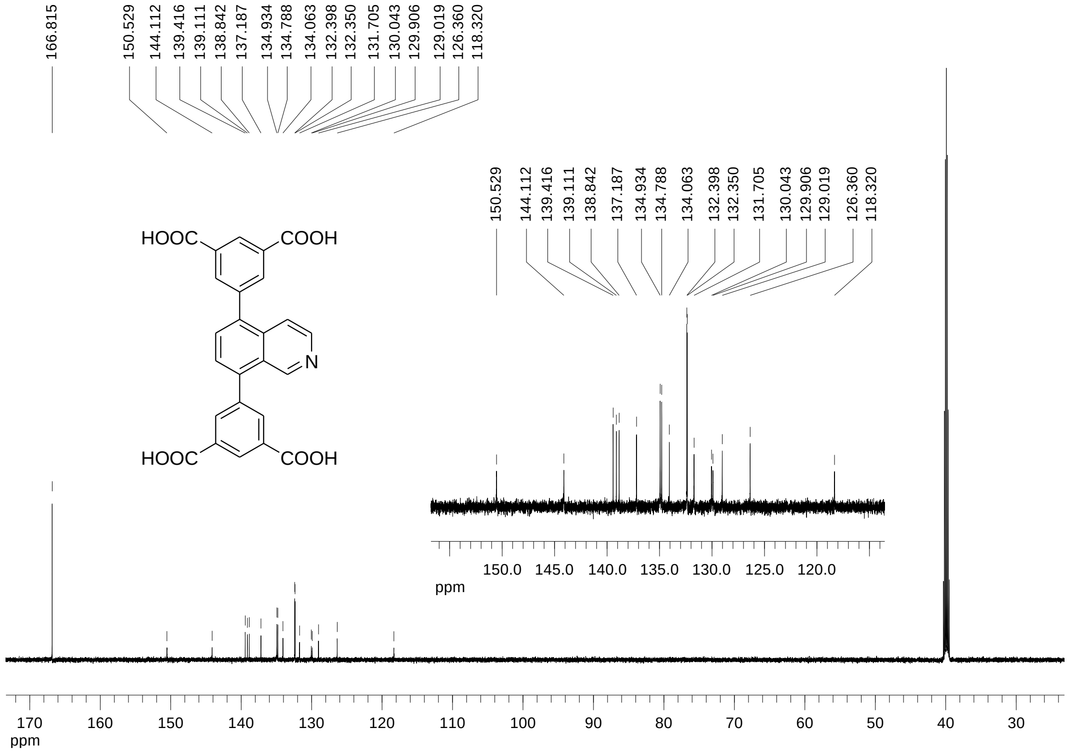
166.815
150.529
144.112
139.416
139.111
138.842
137.187
134.934
134.788
134.063
132.398
132.350
131.705
130.043
129.906
129.019
126.360
118.320
HOOC
COOH
N
HOOC
COOH
150.0
145.0
140.0
135.0
130.0
125.0
120.0
ppm
170
160
150
140
130
120
110
100
90
80
70
60
50
40
30
ppm

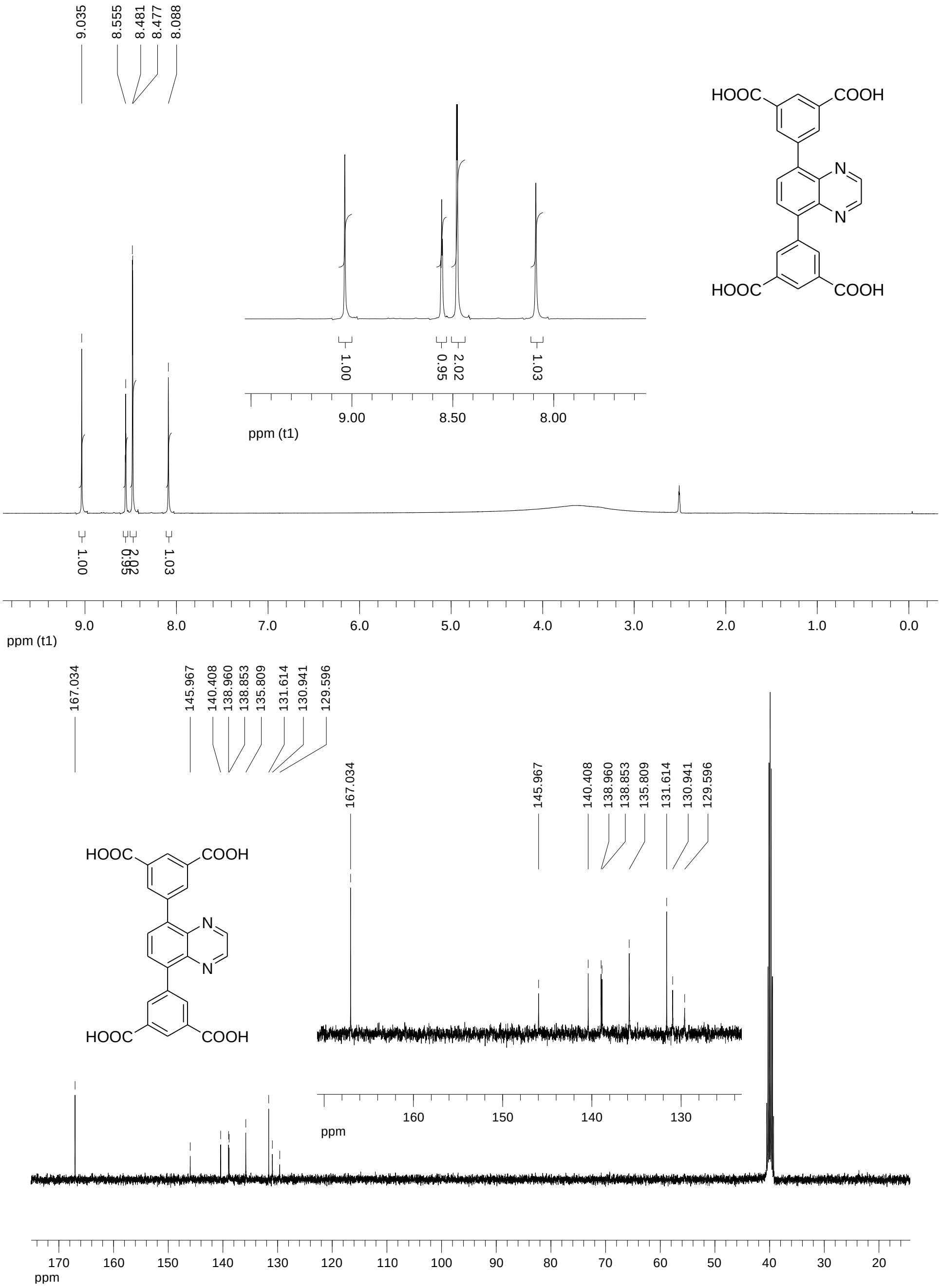

Figure S12. ^{1}H NMR and ^{13}C NMR spectra of the organic linkers in DMSO-d_6.

Table S1. Comparison of the textural properties of **ZJNU-43a**, **ZJNU-44a and ZJNU-45a**.

MOFs	S_{BET} (m^2 g^{-1})	$S_{Langmuir}$ (m^2 g^{-1})	V_p (cm^3 g^{-1})	D_c (g cm^{-3})
ZJNU-43a	2243	2516	0.8943	0.7483
ZJNU-44a	2314	2576	0.9158	0.7471
ZJNU-45a	2232	2473	0.8774	0.7544

Table S2. Langmuir parameters for adsorption of CO_2, CH_4, and N_2 in **ZJNU-43a**. These isotherm fits are based on data at 273 K and 296 K.

	q_{sat} (mol kg^{-1})	b_0 (Pa^{-1})	E (kJ mol^{-1})
CO_2	21	2.63×10^{-10}	22.7
CH_4	7.7	7.56×10^{-9}	13.3
N_2	6.9	5.63×10^{-8}	6

Table S3. Langmuir parameters for adsorption of CO_2, CH_4, and N_2 in **ZJNU-44a**. These isotherm fits are based on data at 273 K and 296 K.

	q_{sat} (mol kg^{-1})	b_0 (Pa^{-1})	E (kJ mol^{-1})
CO_2	24	1.77×10^{-9}	17.9
CH_4	22.5	2.91×10^{-10}	18.3
N_2	10	1.27×10^{-9}	14.2

Table S4. Langmuir parameters for adsorption of CO_2, and CH_4 in **ZJNU-45a**. These isotherm fits are based on data at 273 K and 296 K.

	q_{sat} (mol kg^{-1})	b_0 (Pa^{-1})	E (kJ mol^{-1})
CO_2	19	2.42×10^{-9}	17.7
CH_4	7.8	1.48×10^{-8}	11.5

Table S5. Langmuir parameters for adsorption of N_2 in **ZJNU-45a**. These isotherm fits are based on data at 296 K.

	q_{sat} (mol kg^{-1})	b (Pa^{-1})
N_2	10	3.8×10^{-7}

Table S6. Crystal data and structure refinement for **ZJNU-43, ZJNU-44** and **ZJNU-45.**

MOFs	**ZJNU-43**	**ZJNU-44**	**ZJNU-45**
Empirical formula	$C_{25}H_{15}NO_{10}Cu_2$	$C_{25}H_{15}NO_{10}Cu_2$	$C_{24}H_{14}N_2O_{10}Cu_2$
Formula weight	616.48	616.48	617.47
Temperature (K)	293(2)	293(2)	293(2)
Wavelength (Å)	1.54184	1.54184	1.54184
Crystal system	Trigonal	Trigonal	Trigonal
Space group	*R*-3m	*R*-3m	*R*-3m
Unit cell dimensions	a = 18.5943(3) b = 18.5943(3) c = 38.7113(6) $\alpha = 90^o$ $\beta = 90^o$ $\gamma = 120^o$	a = 18.6463(4) b = 18.6463(4) c = 38.5563(11) $\alpha = 90^o$ $\beta = 90^o$ $\gamma = 120^o$	a = 18.5565(4) b = 18.5565(4) c = 38.6189(8) $\alpha = 90^o$ $\beta = 90^o$ $\gamma = 120^o$
Volume ($Å^3$)	11591.2(3)	11609.4(5)	11516.6(4)
Z	9	9	9
Calculated density (g cm^{-3})	0.7947	0.7935	0.8012
Absorption coefficient (mm^{-1})	1.225	1.272	1.320
F(000)	2322	8262	2934
θ range for data collection (^{o})	2.97 to 73.93	2.97 to 74.29	2.98 to 73.88
Limiting indices	$-23 \le h \le 21$, $-22 \le k \le 23$, $-41 \le l \le 47$	$-22 \le h \le 14$, $-20 \le k \le 23$, $-43 \le l \le 47$	$-15 \le h \le 22$, $-16 \le k \le 20$, $-42 \le l \le 47$
Reflections collected / unique	19641 / 2856 [R_{int} = 0.0364]	14539 / 2856 [R_{int} = 0.0450]	14548 / 2821 [R_{int} = 0.0305]
Completeness to θ	θ = 73.93, 99.5 %	θ = 74.29, 98.7 %	θ = 73.88, 98.6 %
Refinement method	Full-matrix least-squares on F^2	Full-matrix least-squares on F^2	Full-matrix least-squares on F^2
Data / restraints / parameters	2856 / 41 / 148	2856 / 36 / 154	2821 / 51 / 155
Goodness-of-fit on F^2	1.239	1.299	1.059
Final R indices [$I > 2\sigma(I)$]	R_1 = 0.0889, wR_2 = 0.2590	R_1 = 0.0944, wR_2 = 0.2761	R_1 = 0.0578, wR_2 = 0.1788
R indices (all data)	R_1 = 0.0969, wR_2 = 0.2763	R_1 = 0.1032, wR_2 = 0.2937	R_1 = 0.0621, wR_2 = 0.1864
Largest diff. peak and hole (e.$Å^{-3}$)	1.475 and -0.661	1.520 and -0.616	0.743 and -0.483
CCDC	1052691	1052692	1055566